The Astrophysical Journal, 808:91 (18pp), 2015 July 20 doi:10.1088/0004-637X/808/1/91
© 2015. The American Astronomical Society. All rights reserved.

MEASURING INFRARED SURFACE BRIGHTNESS FLUCTUATION DISTANCES WITH *HST* WFC3: CALIBRATION AND ADVICE*

Joseph B. Jensen[1], John P. Blakeslee[2], Zachary Gibson[1], Hyun-chul Lee[3], Michele Cantiello[4], Gabriella Raimondo[4], Nathan Boyer[5], and Hyejeon Cho[6]
[1] Utah Valley University, Orem, UT 84058, USA; jjensen@uvu.edu
[2] NRC Herzberg Astrophysics, Victoria, British Columbia, Canada
[3] The University of Texas Rio Grande Valley, Edinburg, TX, USA
[4] INAF-Osservatorio Astronomico di Teramo, Teramo, Italy
[5] Brigham Young University, Provo, UT, USA
[6] Department of Astronomy and Center for Galaxy Evolution Research, Yonsei University, Seoul 120-749, Korea
Received 2015 May 4; accepted 2015 June 8; published 2015 July 22

ABSTRACT

We present new calibrations of the near-infrared (near-IR) surface brightness fluctuation (SBF) distance method for the F110W (J_{110}) and F160W (H_{160}) bandpasses of the Wide Field Camera 3 Infrared Channel (WFC3/IR) on the *Hubble Space Telescope*. The calibrations are based on data for 16 early-type galaxies in the Virgo and Fornax clusters observed with WFC3/IR and are provided as functions of both the optical ($g_{475}-z_{850}$) and near-infrared ($J_{110}-H_{160}$) colors. The scatter about the linear calibration relations for the luminous red galaxies in the sample is approximately 0.10 mag, corresponding to a statistical error of 5% in distance. Our results imply that the distance to any suitably bright elliptical galaxy can be measured with this precision out to about 80 Mpc in a single-orbit observation with WFC3/IR, making this a remarkably powerful instrument for extragalactic distances. The calibration sample also includes much bluer and lower-luminosity galaxies than previously used for IR SBF studies, revealing interesting population differences that cause the calibration scatter to increase for dwarf galaxies. Comparisons with single-burst population models show that as expected, the redder early-type galaxies contain old, metal-rich populations, while the bluer dwarf ellipticals contain a wider range of ages and lower metallicities than their more massive counterparts. Radial SBF gradients reveal that IR color gradients are largely an age effect; the bluer dwarfs typically have their youngest populations near their centers, while the redder giant ellipticals show only weak trends and in the opposite sense. Because of the population variations among bluer galaxies, distance measurements in the near-IR are best limited to red early-type galaxies. We conclude with some practical guidelines for using WFC3/IR to measure reliable SBF distances.

Key words: distance scale – galaxies: clusters: individual (Virgo, Fornax) – galaxies: distances and redshifts – galaxies: elliptical and lenticular, cD – galaxies: stellar content

1. INTRODUCTION

1.1. Distance Measurements in the Big Picture

Accurate distance measurement is central to both astrophysics and cosmology. Reliable distances are needed to convert observed properties of galaxies (fluxes and angular sizes) into absolute physical quantities such as luminosities, masses, ages, star formation rates, and dynamical timescales. In the local universe where peculiar velocities are significant, the distance estimate is often a major source of uncertainty on these physical properties. For instance, a recent review article on supermassive black holes (Kormendy & Ho 2013) notes that for many galaxies, the errors in the central black hole masses are dominated by the uncertainty in distance; yet, many authors neglect to include this important contribution to the uncertainty.

In the field of cosmology, the acceleration of the cosmic expansion was first revealed by accurate distance measurements of Type Ia supernovae (Riess et al. 1998; Perlmutter et al. 1999). The supernova distance estimates, combined with flatness constraints for the universe provided by the cosmic microwave background (CMB) power spectrum, are primarily responsible for inaugurating a new era of "precision cosmology," central to which is the conclusion that the mass-energy budget of the universe is dominated by "dark energy." Now, with the exquisite constraints on the CMB power spectrum at $z \sim 1100$ (e.g., Bennett et al. 2013; Planck Collaboration 2015) and measurements of the baryon acoustic oscillation scale at intermediate redshift (e.g., Eisenstein et al. 2005; Blake et al. 2011), there has been a new effort to determine the local value of the Hubble constant H_0 to a precision of 1% (Riess et al. 2011; Freedman et al. 2012). As discussed in the foregoing references, this level of precision is required for firm simultaneous constraints on cosmic geometry, the dark energy equation of state, and the number of neutrino species.

Of course, the value of H_0 has been controversial for decades, primarily owing to systematic calibration errors (e.g., Freedman & Madore 2010). Determining H_0 with a total uncertainty of no more than 1% remains beyond the ability of any single distance measurement technique. In order to achieve the required level of precision, it is helpful to have multiple high-precision distance indicators to provide robust constraints on the contributions from systematic errors.

The surface brightness fluctuation (SBF) method provides a measurement of the mean brightness of the red giant branch stars in an early-type galaxy even though individual stars cannot be resolved (Tonry & Schneider 1988). It was introduced as a way to estimate distances with ~10%

* Based on observations with the NASA/ESA *Hubble Space Telescope*, obtained at the Space Telescope Science Institute, which is operated by the Association of Universities for Research in Astronomy, Inc., under NASA contract NAS 5-26555. These observations are associated with Programs #11712, #11570, and #11691.

uncertainty out to about 20 Mpc from ground-based astronomical images (see Tonry et al. 1990). More recent applications have shown substantial improvements in both the precision of the method and depth to which it can be applied (see the reviews by Blakeslee 2012 and Fritz 2012), so that it has become one of a small number of methods capable of making a significant contribution to the problem of constraining H_0 to 1%. In the following sections, we discuss these recent developments with the method and the need for a new calibration at near-infrared (near-IR) wavelengths.

1.2. The Key Role of the Hubble Space Telescope (HST)

The latest revolution in our knowledge of the extragalactic distance scale (decreasing the uncertainty from nearly a factor of two to less than 10%) has resulted primarily from observations made with the *HST*. Starting in the mid-1990s, the *HST* was used to measure light curves for samples of Cepheid variable stars in late-type galaxies out to ~20 Mpc, mostly as part of the Key Project on the Distance Scale (e.g., Freedman et al. 1994; Ferrarese et al. 1996; Kelson et al. 1996; Saha et al. 1996, 1997; Silbermann et al. 1999). The resulting Cepheid distance estimates were used to calibrate various secondary distance indicators and thereby derive the value of the Hubble constant H_0 (Ferrarese et al. 2000; Gibson et al. 2000; Mould et al. 2000; Sakai et al. 2000). The resulting value of H_0 from the Key Project was 72 ± 8 km s^{-1} Mpc^{-1} (Freedman et al. 2001) where the total uncertainty includes both random and systematic contributions. More recent Cepheid-based estimates are very similar to this value, but with reduced uncertainties of 3% to 4% (Riess et al. 2011; Freedman et al. 2012; Sorce et al. 2012).

The excellent angular resolution and photometric stability of *HST* has also made it possible to measure the SBF with far better precision and to much larger distances than was possible from the ground. For instance, Jensen et al. (2001) calibrated the SBF method for the near-IR F160W bandpass of the NICMOS NIC2 camera on *HST* (Thompson et al. 1999) and measured SBF distances to 16 galaxies beyond 40 Mpc, including the first SBF distances reaching beyond 100 Mpc. Stellar population effects on the NICMOS F160W SBF magnitudes were explored in detail by Jensen et al. (2003) using a larger sample of 65 galaxies. In general, the SBF absolute magnitude in a given bandpass depends on stellar population and must be calibrated using a population indicator, typically a broadband color.

Following the installation of the Advanced Camera for Surveys (ACS) on *HST*, Mei et al. (2005b) produced the first calibration of the SBF method for the ACS Wide Field Channel (ACS/WFC) using F475W (g_{475}) and F850LP (z_{850}) data for 84 galaxies from the ACS Virgo Cluster Survey (ACSVCS; Côté et al. 2004). In that work, the z_{850} SBF measurements were calibrated for stellar population variations based on the observed $(g_{475}-z_{850})$ color; the resulting distances enabled the first clear resolution of the depth of the Virgo cluster and provided constraints on its triaxial structure (Mei et al. 2007). In other studies based on ACS/WFC observations, Cantiello et al. (2005, 2007) measured multi-band SBF and color gradients in 21 galaxies, and Biscardi et al. (2008) made the first optical SBF measurements beyond 100 Mpc. As part of the ACS Fornax Cluster Survey (ACSFCS; Jordán et al. 2007), Blakeslee et al. (2009) refined the SBF calibration for the ACS F850LP bandpass and determined the relative distance of the Virgo and Fornax clusters to a precision of 1.7%. Additional ACS/WFC SBF measurements and a new calibration for the F814W bandpass were published by Blakeslee et al. (2010). The launch of Wide Field Camera 3 with its powerful IR channel (WFC3/IR) has greatly increased the distance to which SBF measurements can be made within a single *HST* orbit. However, the method must first be calibrated for selected WFC3/IR passbands as done previously for NICMOS and ACS; this is the primary goal of the present work.

1.3. SBF Measurements in the Infrared

The development of new infrared detectors in the 1990s allowed researchers to successfully apply the SBF techniques to IR images for the first time (Luppino & Tonry 1993; Pahre & Mould 1994; Jensen et al. 1996). Because the SBF signal is dominated by the most luminous stars in a population, and these tend to be quite red for evolved galaxies, SBF magnitudes are much brighter in the near-IR than at optical wavelengths. Additionally, extinction by dust (both in our Galaxy and in the target galaxy) is much lower at near-IR wavelengths. Depending on how it is distributed, dust can either reduce the fluctuation signal (as for a uniform screen of foreground dust in the Galaxy), or, more commonly, bias the fluctuation signal toward higher amplitudes and shorter SBF distances, as would occur if dusty regions were clumpy on scales comparable to the size of the point-spread function (PSF). Clumpy dust is often associated with recent star formation, and bright young stars seriously bias SBF measurements as well. The contrast between the fluctuations and other point-like sources (globular clusters and background galaxies) is also higher in the near-IR bands, reducing yet another source of uncertainty in the SBF measurement. While the background in the IR is higher than at optical wavelengths, the increased strength of the SBF signal more than compensates, especially from space, where the thermal background at 1.1 and 1.6 μm is not significant. The benefit of the much lower background, combined with the excellent image quality and a very stable PSF, usually makes near-IR SBF measurements with *HST* much more accurate than measurements from ground-based facilities.

However, the calibration of the SBF magnitudes as a function of stellar population is potentially more complicated in the near-IR. As noted above, the trend of SBF magnitude with galaxy color is used for calibrating the SBF distance measurements, both at optical and IR wavelengths. At optical wavelengths, the effects of age and metallicity variations on the SBF calibration relations are largely degenerate, but this degeneracy begins to break down in near-IR, and this can reveal interesting differences in the stellar populations of galaxies. Bluer elliptical and S0 galaxies typically show signs of intermediate-age populations, and the asymptotic giant branch (AGB) stars associated with those populations produce brighter fluctuations (Jensen et al. 2003; Mieske et al. 2003, 2006). The stellar population variations may therefore produce more scatter in IR SBF distance calibration, but the brightness of the fluctuations at these wavelengths makes them measurable to much larger distances; thus, it is worth characterizing the behavior and limits of the calibration as well as possible.

In this paper we report the results of a study to calibrate the IR SBF distance measurement technique using new SBF

Table 1
Galaxy Properties

Galaxy	Cluster[a]	Type[b]	m_B[c] (mag)	R_e[d] (arcsec)	M_B[e] (mag)	R_e[f] (kpc)	A_J[g] (mag)	Alt ID[h]
IC 1919	F	dS0	13.5	21.2	−18.1	2.06	0.010	FCC 43
IC 2006	F	E1	12.2	18.9	−19.4	1.84	0.008	⋯
NGC 1344	F	E5	11.3	33.2	−20.3	3.22	0.013	NGC 1340
NGC 1374	F	E0	11.9	29.2	−19.7	2.83	0.010	FCC 147
NGC 1375	F	S0	13.6	13.2	−18.0	1.28	0.010	FCC 148
NGC 1380	F	S0	11.3	30.3	−20.3	2.94	0.012	FCC 167
NGC 1399	F	E0	10.6	114.6	−21.0	11.11	0.009	FCC 213
NGC 1404	F	E2	10.9	22.9	−20.7	2.22	0.008	FCC 219
IC 3025	V	dS0	14.8	9.8	−16.4	0.78	0.015	VCC 21
IC 3032	V	dE2	14.7	9.1	−16.6	0.73	0.026	VCC 33
IC 3487	V	dE6	14.8	9.3	−16.4	0.74	0.015	VCC 1488
IC 3586	V	dS0	14.5	20.2	−16.7	1.61	0.032	VCC 1695
NGC 4458	V	E1	12.9	20.4	−18.2	1.63	0.017	VCC 1146
NGC 4472	V	E2	9.3	210.8	−21.9	16.87	0.016	VCC 1226
NGC 4489	V	S0	12.8	37.1	−18.4	2.97	0.020	VCC 1321
NGC 4649	V	E2	9.8	98.1	−21.4	7.85	0.019	VCC 1978

Notes.
[a] Cluster: *V* for Virgo and *F* for Fornax.
[b] Morphological type from the ACSVCS (Côté et al. 2004) and ACSFCS (Jordán et al. 2007).
[c] Apparent *B*-band magnitude (Vega).
[d] Effective radius in arcseconds, determined from the ACS and/or SDSS imaging (Ferrarese et al. 2006; Chen et al. 2010; P. Côté 2015, private communication).
[e] Absolute *B* magnitude (Vega), corrected for Galactic extinction, and assuming distances of 16.5 and 20.0 Mpc for galaxies in Virgo and Fornax, respectively.
[f] Effective radius in kpc, assuming same Virgo and Fornax distances as above.
[g] Galactic extinction (Vega mag) in *J*-band, from Schlafly & Finkbeiner (2011).
[h] Alternate names from Virgo and Fornax Cluster Catalogs (Binggeli et al. 1985; Ferguson 1989), or alternate NGC designation in the case of NGC 1344.

measurements in the F110W (J_{110}) and F160W (H_{160}) bandpasses of WFC3/IR on *HST*. The calibration sample includes 16 galaxies spanning a wide range in galaxy luminosity and color. The following section describes the observations and sample in more detail. Section 3 discusses the data reductions and SBF measurements. New SBF calibrations in J_{110} and H_{160} are presented in Section 4, while implications of the SBF measurements for the galaxy stellar populations are discussed in Section 5. We provide our recommendations for measuring SBF distances with WFC3/IR in Section 6, before concluding with a summary.

2. WFC3/IR OBSERVATIONS

In order to calibrate the SBF method for WFC3/IR, we selected 16 early-type galaxies, eight in each of the Virgo and Fornax clusters, that already had high-quality ACS SBF measurements in z_{850} and $(g_{475}-z_{850})$ colors (Blakeslee et al. 2009). Table 1 lists the properties of the galaxies that were targeted in *HST* program GO-11712 (PI: J. Blakeslee). The galaxies were chosen to cover the full color range of the ACSVCS and ACSFCS samples so that the resulting calibration would be as generally applicable as possible. Moreover, the NICMOS SBF calibration exhibited increased scatter for bluer galaxies (Jensen et al. 2003), as have ground-based *I*-band SBF measurements (Mieske et al. 2006); exploring a broad color range should help us understand where the WFC3/IR calibration becomes less reliable.

Each of these 16 galaxies were observed for one orbit, split approximately equally between the J_{110} and H_{160} filters, with four dithered exposures in each filter and total exposure times varying with target visibility. The same dither pattern was used for each galaxy.

For this study we also downloaded archival WFC3/IR H_{160} data for NGC 4258 (GO-11570, PI: A. Riess) and NGC 1316 (GO-11691, PI: P. Goudfrooij). NGC 4258 is a late-type galaxy with a H_2O masers in Keplerian orbits around a central black hole, enabling a geometric estimate of the distance (Greenhill et al. 1995; Miyoshi et al. 1995; Herrnstein et al. 1999). While not ideal for SBF analysis, the importance of this galaxy to the absolute calibration of the extragalactic distance scale makes it an important target worthy of a trial SBF measurement. NGC 1316 is an early-type S0 galaxy in the Fornax cluster with extensive dust and signs of recent merging. Although it is also a poor SBF candidate, it is a useful comparison galaxy for this study because it has hosted *four* Type Ia supernovae.

Tables 2 and 3 list the exposure times and sky brightnesses for the all the J_{110} and H_{160} observations used in this study. Additional information in these tables is discussed in the following sections.

3. SBF MEASUREMENTS

The spatial fluctuations in the surface brightness of a smoothly distributed population of stars, as found in elliptical and lenticular galaxies, arise due to the Poisson statistics of the discrete stars making up the galaxy, even when the stars cannot be resolved or detected individually (Tonry & Schneider 1988). The SBF amplitude scales inversely with the square of the

Table 2
J_{110} SBF Measurements

Galaxy	Exposure (s)	Background (AB mag arcsec^{-2})	Annulus (arcseconds)	<gal/sky>[a] average	gal/sky range	SBF S/N[b] $(P_0 - P_r)/P_1$	$\overline{m}_{110}$[c] (AB mag)
Fornax							
IC 1919	997	21.74	8–33	1.3	0.9–2.6	33	28.31 ± 0.05
IC 2006	997	22.40	4–33	12	6–58	43	28.63 ± 0.05
NGC 1344	997	22.10	4–33	19	11–85	83	28.37 ± 0.05
NGC 1374	997	22.02	4–33	10	5–48	47	28.55 ± 0.06
NGC 1375	1197	22.64	4–33	5.8	3.1–27	59	28.19 ± 0.05
NGC 1380	1197	22.22	6–33	29	19–124	49	28.51 ± 0.04
NGC 1399	1197	22.15	4–33	41	23–194	52	28.79 ± 0.05
NGC 1404	997	22.04	4–33	32	17–173	47	28.68 ± 0.06
Virgo							
IC 3025	997	21.84	8–17	0.8	0.8	17	28.36 ± 0.06
IC 3032	997	21.81	8–17	0.8	0.8	34	27.95 ± 0.07
IC 3487	997	21.84	4–33	0.4	0.2–2.5	27	28.16 ± 0.10
IC 3586	997	22.17	4–33	0.8	0.5–3.6	34	28.05 ± 0.08
NGC 4458	997	22.12	4–67	4.4	0.5–22	47	28.01 ± 0.05
NCG 4472	748	22.10	4–67	68	17–249	40	28.38 ± 0.06
NGC 4489	997	22.23	8–67	4.5	0.6–8	58	27.81 ± 0.06
NGC 4649	997	22.10	4–67	61	14–250	43	28.44 ± 0.06
Supernova Host							
NGC 1316	1396	22.08	33–67	15	8–34	166	28.26 ± 0.07

Notes.
[a] Weighted average ratio of the galaxy surface brightness to sky background surface brightness within the measurement region.
[b] Weighted average ratio of the SBF fluctuation power to the white noise component P_1 of the spatial power spectrum.
[c] SBF magnitudes have been corrected for Galactic extinction using values from Schlafly & Finkbeiner (2011).

Table 3
H_{160} SBF Measurements

Galaxy	Exposure (s)	Background (AB mag arcsec^{-2})	Annulus (arcseconds)	⟨gal/sky⟩[a] average	gal/sky range	SBF S/N[b] $(P_0 - P_r)/P_1$	$\overline{m}_{160}$[c] (AB mag)
Fornax							
IC 1919	997	21.90	8–33	1.8	1.3–3.8	43	27.55 ± 0.06
IC 2006	997	22.13	4–33	12	6–59	59	27.86 ± 0.04
NGC 1344	997	21.90	4–33	20	12–91	77	27.52 ± 0.05
NGC 1374	748	21.95	4–33	12	6–59	45	27.88 ± 0.05
NGC 1375	1197	22.36	4–33	5.5	2.9–27	62	27.42 ± 0.05
NGC 1380	1197	21.95	6–67	29	19–120	71	27.80 ± 0.05
NGC 1399	1197	21.95	4–33	46	25–220	52	28.03 ± 0.04
NGC 1404	997	22.07	4–33	43	22–235	50	27.94 ± 0.06
Virgo							
IC 3025	997	21.76	8–17	0.3	0.3	27	27.72 ± 0.07
IC 3032	997	21.86	8–17	1.0	1.0	17	26.94 ± 0.09
IC 3487	997	21.75	4–33	0.4	0.2–2.7	27	27.42 ± 0.09
IC 3586	997	22.01	4–33	0.9	0.5–3.8	38	27.26 ± 0.04
NGC 4458	997	21.94	4–67	4.7	0.5–23	56	27.35 ± 0.05
NCG 4472	748	21.83	4–67	71	17–258	47	27.59 ± 0.05
NGC 4489	997	22.07	8–67	4.8	0.6–8	67	27.10 ± 0.05
NGC 4649	997	21.90	4–67	68	15–283	67	27.63 ± 0.05
Supernova Host							
NGC 1316	2796	21.85	33–67	21	9–36	111	27.35 ± 0.07
Maser Host							
NGC 4258	2012	21.91	irreg.	10	47	47	25.30 ± 0.06

Notes.
[a] Weighted average ratio of the galaxy surface brightness to sky background surface brightness within the measurement region.
[b] Weighted average ratio of the SBF fluctuation power to the white noise component of the spatial power spectrum.
[c] SBF magnitudes have been corrected for Galactic extinction using values from Schlafly & Finkbeiner (2011).

distance: nearby galaxies appear "bumpy" compared to more distant galaxies, where more stars are sampled by each resolution element and the $\sqrt{N}$ variation between regions is therefore a smaller fraction of the total number of stars. The fluctuations, which are dominated by the most luminous stars in a population, are blurred by the PSF; additional contributions to

the fluctuation signal arise from clumpy dust, globular clusters, background galaxies, and foreground stars. The process of making an SBF measurement consists of extracting and fitting the spatial Fourier power spectrum of the stellar fluctuations convolved with the PSF power spectrum and removing the contributions from extraneous sources. The resulting fluctuation power is used to compute the fluctuation magnitude.

Procedures for measuring the SBF have been described in detail by several authors (e.g., Tonry et al. 1990, 1997; Blakeslee et al. 1997; Jensen et al. 1998; Mei et al. 2005a; Fritz 2012). The description here provides a concise overview of the process steps that are either unique to this study or are particularly relevant to the WFC3/IR SBF measurements.

3.1. Data Reduction

The first step in the SBF data reduction process involves producing a calibrated, combined, and background-subtracted image ready for further SBF analysis. We used the images from the *HST* archive reduced using the standard pipeline through the flat-fielding stage (*flt* files). From that point, we adopted a reduction procedure that differs from the standard pipeline.

We combined the individual flat-fielded exposures using integer pixel shifts after fitting each image for background and identifying cosmic rays; in order to avoid introducing correlated noise between pixels, fractional pixel registration was *not* used. Using integer pixel shifts results in slightly lower spatial resolution in the combined image, but preserves the independence of noise from pixel to pixel, which is important for fitting the SBF power spectrum.

In a second difference from the standard pipeline reduction, the clean combined images were *not* corrected for the WFC3/IR geometrical distortion nor combined using *astrodrizzle*. Our analysis therefore includes the ∼10% difference in plate scale between the x and y axes, causing our images to appear somewhat narrower horizontally than they do on the sky (Figure 1). The SBF procedure involves taking the spatial Fourier power spectrum, and correlated noise between pixels resulting from fractional pixel shifts and interpolated pixel values when correcting for geometrical distortion can produce a slope in the white noise component of the power spectrum.

Finally, we chose not to apply the correction to pixel size in the y-axis of WFC3/IR images. The pixel map correction usually used for WFC3/IR corrects for PSF variations but is inappropriate for extended objects. The WFC3/IR focal plane is tilted and the size (area) of the pixels on the sky varies by ∼8% from the center to the upper and lower edges of the frame (Kalirai et al. 2010). When the data are divided by the flat field image (as is done for the *flt* files in the *HST* archive), the varying pixel sensitivity is removed, effectively making the pixels equally sensitive to uniform illumination. Flattening the images in this way creates a variation in sensitivity for point sources from the center to the top and bottom edges that is usually corrected in the pipeline data reduction process using *astrodrizzle*. Since we are interested in accurately measuring the surface brightnesses of the galaxies and avoiding correlated noise between pixels, we chose not to correct for pixel size variation in our SBF data reduction process. The practical effect of this decision is that the PSF at the extreme upper and lower regions of the image does not match the PSF near the center. We have carefully chosen PSF reference stars from the same vertical region of the field of view as the galaxies being analyzed (usually very near the center) to avoid any systematic offset between the PSF photometric normalization or power spectrum shape and the galaxy fluctuations. The chosen PSF stars were all unresolved, isolated from other bright objects, and much brighter than the globular cluster population.

3.2. Measuring Fluctuations

SBF measurements are made by fitting the Fourier spatial power spectrum of the stellar fluctuations in a given region of a galaxy with the normalized power spectrum of the PSF. There are several steps to produce the spatial power spectrum: (i) the background level is estimated and subtracted; (ii) extraneous objects (globular clusters, background galaxies, and dusty regions) are identified, measured, and masked; (iii) a smooth isophotal model is fitted to the galaxy profile and subtracted; (iv) isolated bright stars are extracted and used to determine the power spectrum of the PSF; (v) the Fourier power spectra are computed for the stellar fluctuations, the masked galaxy profile, and the PSF; and (vi) the power spectrum of the data is fitted and normalized to determine the SBF power in units of flux, with the power from undetected globular clusters and galaxies subtracted, from which a fluctuation magnitude is computed in the established way (e.g., Jensen et al. 1998; Tonry & Schneider 1988; Mei et al. 2005a).

It is important to accurately measure and subtract the IR background before computing fluctuation magnitudes. Estimating the background level was done in an iterative process of cross-checking values measured in different ways. For the small galaxies, we measured the flux in the corners of the frames. For the larger ellipticals, we also determined the background using the best fit to a $r^{1/4}$ profile for each galaxy. These estimates were then compared to a measurement of the background made by iteratively computing a smooth model for each galaxy and looking at the residual background in the field of view. By adjusting the sky level offset, we optimized the galaxy models such that the residual background was not systematically positive or negative. The difference between the sky values determined using the different methods was used as an estimate of the uncertainty in the sky level, and the SBF analysis was repeated to determine the uncertainty in fluctuation magnitude due to sky level uncertainty. The SBF magnitude is normalized by the mean galaxy brightness at the location of the SBF measurement. For the smaller galaxies with the lowest surface brightness (see Figure 1), the background level was most accurately measured. For the largest galaxies that extend beyond the limits of the field of view, the background was most difficult to measure accurately, but its influence on the SBF measurement was also minimal. The uncertainty in the SBF magnitude is therefore relatively insensitive to the uncertainty in the background measurement.

Typical background levels at J_{110} were $1.3\,e^-\,s^{-1}\,pix^{-1}$, or 22.10 ± 0.23 AB mag arcsec^{-2}; at H_{160} we measured $0.67\,e^-\,s^{-1}\,pix^{-1}$, or 21.95 ± 0.15 AB mag arcsec^{-2} (see Tables 2 and 3). These sky values were found to be consistent with published empirical measurements of the *HST* IR background, which is dominated by scattered zodiacal light in the solar system (Pirzkal 2014). The J_{110} background levels were also affected by the diffuse upper-atmosphere He emission line at 1.083 μm (Brammer et al. 2014). While very few individual exposures were strongly affected, the residual background variation among the data is larger at J_{110} than at H_{160}. The background variability between observations of different

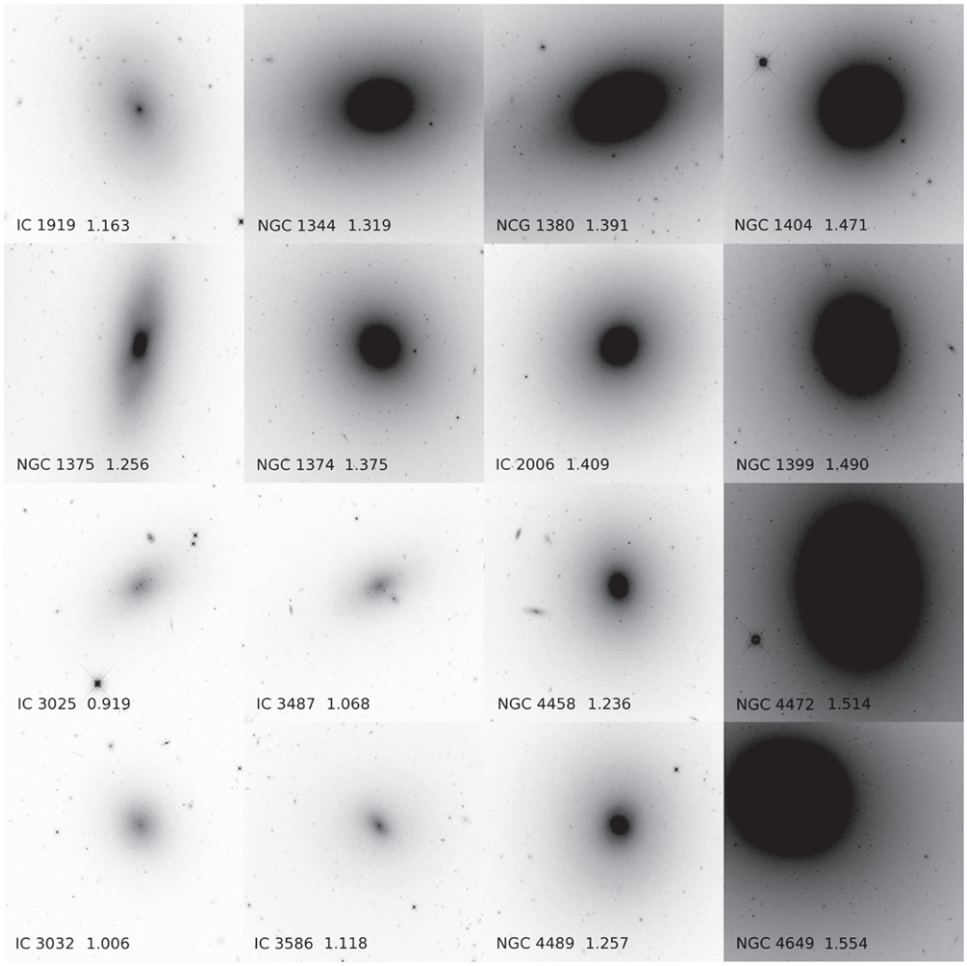


Figure 1. Fornax (top two rows) and Virgo cluster galaxies (bottom two rows). Each image is displayed with the background subtracted and using the same upper and lower limits and logarithmic stretch, within the same field of view 100 arcsec on a side. The bluer galaxies are on the left and the redder giant ellipticals are on the right. Measured values of $(g_{475}-z_{850})$ (AB) are shown next to the galaxy labels.

galaxies (see Tables 2 and 3) is not directly related to the uncertainty in the background measurement for a particular galaxy, which was determined independently for each galaxy.

After the background had been subtracted, we then identified and masked any non-fluctuation point sources in the field of view. Background galaxies and globular clusters were identified and their brightnesses measured using the SExtractor software (Bertin & Arnouts 1996) and adopting aperture corrections taken from the WFC3 instrument webpage.[7] We started by making an initial fit to the galaxy and subtracting it to make it easier for SExtractor to identify and measure all the compact objects in the field (we used a noise model for SExtractor that accounts for the subtracted galaxy and prevents the software from confusing the stellar fluctuations with globular clusters). Using the SExtractor output, we then created a fit to the luminosity functions of the globular clusters and background galaxies. For most of the galaxies, we used a Gaussian of width 1.2 mag to fit the luminosity functions; we found that a width of 1.35 mag fit better for NGC 1399 and NGC 4472. We adopted a luminosity function peak absolute magnitude of $M_V = -7.40$, $M_J = -8.26$, and $M_H = -8.29$ (e.g., Frogel et al. 1978; Harris 2001, p. 223). The background galaxies are assumed to follow a power law distribution with a power law slope of 0.25, which for most of our observations results in a normalization of about one to two galaxies per square arcsec at 34.50 mag AB (Retzlaff et al. 2010; Windhorst et al. 2011). These fits allowed us to integrate the contribution to the SBF signal fainter than the completeness limit and correct the final SBF magnitude accordingly. A mask was then created from the list of objects that removed all objects brighter than the limiting cutoff magnitude.

The next step was to fit a final smooth model to the galaxy profile with the sky and point sources removed. We used an iterative procedure of fitting elliptical isophotes to the galaxy surface brightness profile, allowing the procedure to adjust the centers, ellipticities, and orientations of the elliptical apertures. This model galaxy was later used to normalize the fluctuation signal.

With the sky background and mean galaxy surface brightness removed and contaminating point sources masked, we then computed the Fourier transform and spatial power spectrum of the data in circular annuli (see Tables 2 and 3 for the sizes of the annular regions). The measurements were repeated using elliptical annuli for the six most elongated galaxies with apparent radial gradients in their SBF magnitudes. The power spectrum was normalized by the mean galaxy luminosity so that the fluctuation amplitude should be the same in each annulus. The purpose of

[7] http://www.stsci.edu/hst/wfc3/phot_zp_lbn

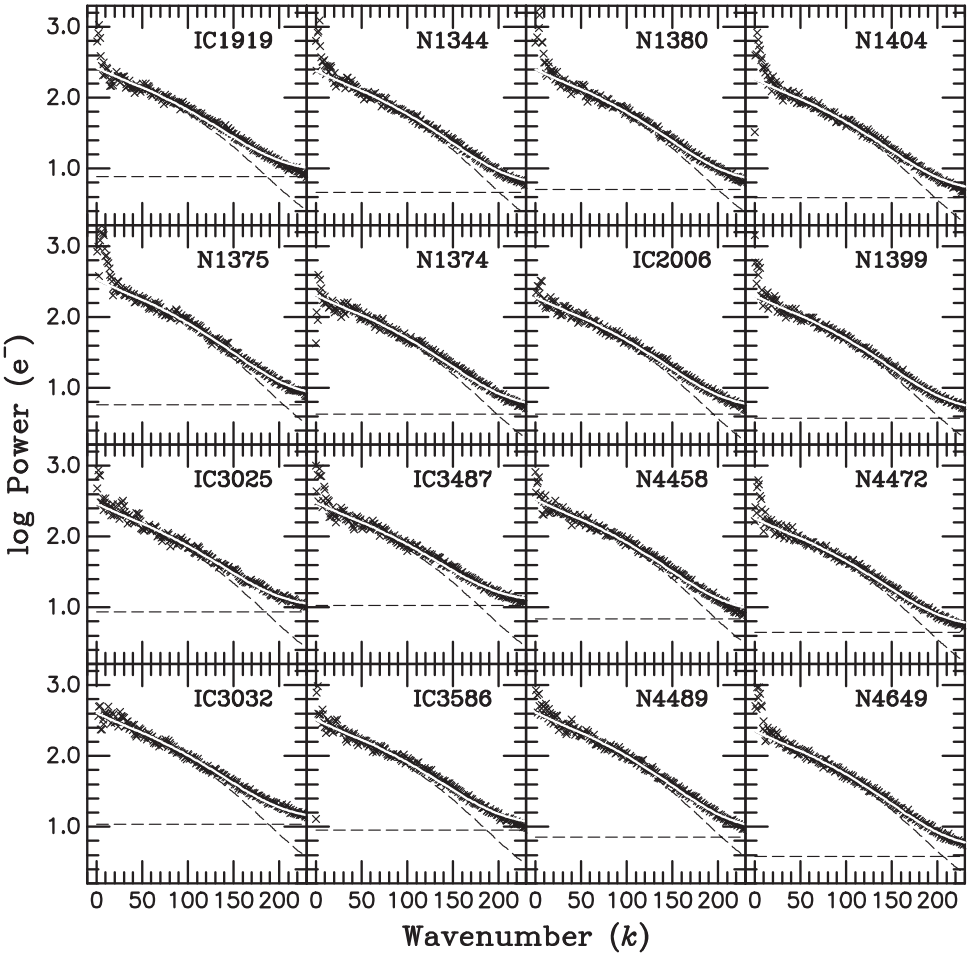


Figure 2. Fits to the spatial power spectra for the 16 galaxies in Fornax and Virgo (superimposed white line). The dashed lines indicate the scaled PSF power spectrum and the white noise (flat) components.

measuring fluctuations in multiple annuli was to look for consistency between regions with varying surface brightness, globular cluster population, and distance from the center. It also allowed us to measure the radial gradients in fluctuation amplitude, and thus the stellar population, as described in Section 5.5.

The measured fluctuation power spectrum is a convolution of the pixel-to-pixel variation in the number of stars and the PSF of the instrument. We therefore require a robust measurement of the PSF power spectrum to determine the fluctuation amplitude. We extracted isolated bright stars from the central region of the detector field of view and computed their power spectra. Because PSF stars are not all uniformly centered on the pixels, there is some variation that naturally arises in the PSF power spectra. To determine which PSF stars best fitted the power spectrum for a particular galaxy, we combined the cleanest and brightest PSF stars from several observations, and then repeated the SBF measurements using a variety of PSF stars. We computed the uncertainty in SBF magnitude attributable to the PSF variations by determining the range of plausible PSF fits based on the shape of the power spectra and the quality of the fits. We then used a common composite PSF to measure SBF consistently in all the galaxies (the same dither pattern was used for all the observations). As an added check on the PSF uniformity and fit quality, we also fitted the observed power spectra to the "Tiny Tim" PSF models[8] (Krist et al. 2011). The Tiny Tim model PSF for each filter was convolved with Gaussians of various widths to construct a library of model PSFs to provide better matches to the data, which had been combined using integer pixel offsets and no geometrical distortion corrections (see Section 3.1). The SBF magnitudes computed using the Tiny Tim model PSFs were then compared to those derived from the combined empirical PSFs and the range of plausible fits was used to determine the uncertainty due to PSF variations (typically 0.04 mag).

Fluctuation magnitudes were computed by fitting the normalized PSF power spectrum to the galaxy power spectrum $P(k) = P_0 E(k) + P_1$, where $E(k)$ is the expectation power spectrum, which includes the smooth galaxy profile and the combined annular region and external object mask, all convolved with the normalized PSF power spectrum (see Figure 2 for power spectra and fit components). The fits excluded the lowest wavenumbers $k < 10$, which are affected by large-scale galaxy and sky subtraction errors. P_1 is the white noise component, which is flat for uncorrelated pixel-to-pixel noise. The scale factor used to best match the data corresponds to the flux in SBF power in units of $e^- s^{-1}$. It is then straight-

[8] http://tinytim.stsci.edu/cgi-bin/tinytimweb.cgi

Table 4
Absolute SBF Magnitudes

Galaxy	$(m-M)$[a]	$(g_{475}-z_{850})$[b]	$(J_{110}-H_{160})$	$\overline{M}_{110}$[c]	$\overline{M}_{110}$[d]	$\overline{M}_{160}$[c]	$\overline{M}_{160}$[d]
Fornax							
IC 1919	31.485 ± 0.073	1.163 ± 0.037	0.223 ± 0.007	−3.18 ± 0.09	−3.20 ± 0.08	−3.94 ± 0.09	−3.96 ± 0.08
IC 2006	31.525 ± 0.086	1.409 ± 0.013	0.263 ± 0.013	−2.90 ± 0.10	−2.88 ± 0.07	−3.67 ± 0.10	−3.65 ± 0.07
NGC 1344	31.603 ± 0.068	1.319 ± 0.007	0.260 ± 0.008	−3.23 ± 0.08	−3.14 ± 0.07	−4.08 ± 0.08	−3.99 ± 0.07
NGC 1374	31.458 ± 0.070	1.375 ± 0.011	0.251 ± 0.014	−2.91 ± 0.09	−2.96 ± 0.08	−3.58 ± 0.09	−3.63 ± 0.07
NGC 1375	31.500 ± 0.072	1.256 ± 0.029	0.224 ± 0.016	−3.31 ± 0.09	−3.32 ± 0.07	−4.08 ± 0.09	−4.09 ± 0.07
NGC 1380	31.632 ± 0.075	1.391 ± 0.007	0.286 ± 0.006	−3.12 ± 0.09	−3.00 ± 0.07	−3.83 ± 0.09	−3.71 ± 0.07
NGC 1399	31.596 ± 0.091	1.490 ± 0.005	0.302 ± 0.012	−2.81 ± 0.10	−2.72 ± 0.07	−3.57 ± 0.10	−3.48 ± 0.07
NGC 1404	31.526 ± 0.072	1.471 ± 0.006	0.292 ± 0.005	−2.85 ± 0.09	−2.83 ± 0.08	−3.59 ± 0.10	−3.57 ± 0.08
Virgo							
IC 3025	31.421 ± 0.130	0.919 ± 0.074	0.183 ± 0.019	−3.06 ± 0.14	−2.73 ± 0.11	−3.70 ± 0.15	−3.37 ± 0.11
IC 3032	30.886 ± 0.133	1.006 ± 0.030	0.184 ± 0.036	−2.94 ± 0.15	−3.14 ± 0.11	−3.95 ± 0.16	−4.15 ± 0.13
IC 3487	31.053 ± 0.134	1.068 ± 0.060	0.132 ± 0.023	−2.89 ± 0.17	−2.93 ± 0.13	−3.63 ± 0.16	−3.67 ± 0.13
IC 3586	31.093 ± 0.080	1.118 ± 0.040	0.188 ± 0.007	−3.04 ± 0.11	−3.04 ± 0.11	−3.83 ± 0.09	−3.83 ± 0.13
NGC 4458	31.063 ± 0.070	1.236 ± 0.049	0.237 ± 0.026	−3.05 ± 0.08	−3.08 ± 0.10	−3.71 ± 0.09	−3.74 ± 0.10
NCG 4472	31.116 ± 0.075	1.514 ± 0.006	0.291 ± 0.013	−2.74 ± 0.10	−2.71 ± 0.10	−3.53 ± 0.09	−3.50 ± 0.10
NGC 4489	30.935 ± 0.069	1.257 ± 0.014	0.226 ± 0.013	−3.13 ± 0.09	−3.28 ± 0.10	−3.84 ± 0.08	−3.99 ± 0.10
NGC 4649	31.082 ± 0.079	1.554 ± 0.006	0.311 ± 0.013	−2.64 ± 0.10	−2.65 ± 0.11	−3.45 ± 0.09	−3.46 ± 0.10
Supernova Host							
NGC 1316	31.606 ± 0.065	1.374 ± 0.007	0.272 ± 0.007	−3.35 ± 0.10	−3.25 ± 0.09	−4.26 ± 0.10	−4.16 ± 0.09
Maser Host							
NGC 4258	29.404 ± 0.048	1.361 ± 0.044	…	…	…	−4.10 ± 0.08	…

Notes. All magnitudes are on the AB system and extinction corrected.
[a] Blakeslee et al. (2009) except NGC 4258, Humphreys et al. (2013).
[b] Galaxy colors from Blakeslee et al. (2009) have been updated to match the apertures used in this study, and corrected for extinction using Schlafly & Finkbeiner (2011).
[c] $\overline{M}$ computed using the individual distance moduli shown in the second column.
[d] $\overline{M}$ computed using average cluster distances of 31.51 mag for Fornax and 31.09 for Virgo. Uncertainties on $\overline{M}$ include the cluster depths of 0.053 mag (Fornax) and 0.085 mag (Virgo).

forward to compute the fluctuation magnitude:

$$\overline{m} = -2.5\log(P_0 - P_r) + M_1,$$

where P_0 is the fluctuation power and P_r is the contribution from point sources fainter than the completeness limit. M_1 is the zero point for the filter+detector (26.8223 AB for J_{110} and 25.9463 AB for H_{160}). The AB magnitude is 0.7595 mag larger than the Vega equivalent at J_{110}, and 1.2514 mag larger than the Vega magnitude at H_{160}. AB magnitudes and colors were corrected for Galactic extinction using the values published by Schlafly & Finkbeiner (2011). The $(g_{475}-z_{850})$ colors from Blakeslee et al. (2009) were adjusted to make them consistent with the Schlafly & Finkbeiner extinction values. Individual sky background levels, exposure times, and SBF signal-to-noise ratio (S/N) values are listed in Tables 2 and 3.

Absolute fluctuation magnitudes $\overline{M}_{110}$ and $\overline{M}_{160}$ (Table 4) were then computed using both individual distance modulus measurements and average cluster distances of $(m-M) = 31.51$ mag for the Fornax cluster and 31.09 for Virgo (all from the optical ACS SBF measurements of Blakeslee et al. 2009). The radial extent of each cluster (0.053 mag for Fornax and 0.085 mag for Virgo) was adopted as the uncertainty on the average cluster distance moduli. The colors originally reported by Blakeslee et al. (2009) were recomputed for the apertures used in this study (circular and elliptical).

There are several sources of uncertainty in the SBF measurement procedure that we quantified by exploring the range of input parameters, as we did for the uncertainty due to the PSF fit. Average values (and ranges) of the uncertainties we measured and adopted for the final SBF measurements are listed in Table 5. Not all sources of uncertainty are completely independent—residual errors in sky subtraction can affect the galaxy or PSF fit, for example—so the total uncertainties listed in Table 4 are not a simple quadrature addition of all sources listed in Table 5; we estimated the fraction of the power spectrum fit (P_0) uncertainty that results from the PSF fit and sky subtraction separately before adding all independent sources of error in quadrature. The distance modulus uncertainties were included in the individual-distance values of $\overline{M}$. The cluster-distance $\overline{M}$ values include the cluster distance dispersion values from Blakeslee et al. (2009) in the total uncertainty.

Table 5
Average Uncertainties

Source	σ (mag)	Range (mag)
Power spectrum fit P_0	0.06	0.04–0.10
PSF fit	0.04	0.026–0.067
Background subtraction	0.01	0.002–0.062
Galaxy subtraction	0.007	0.001–0.022
$(g_{475}-z_{850})$ color uncertainty	0.025	0.005–0.074
$(J_{110}-H_{160})$ color uncertainty	0.013	0.002–0.036
Distance modulus (individual)	0.086	0.068–0.134
Distance modulus (Virgo)	0.085	0.085
Distance modulus (Fornax)	0.053	0.053
Total statistical $\overline{M}$ uncertainty	0.10	0.08–0.17

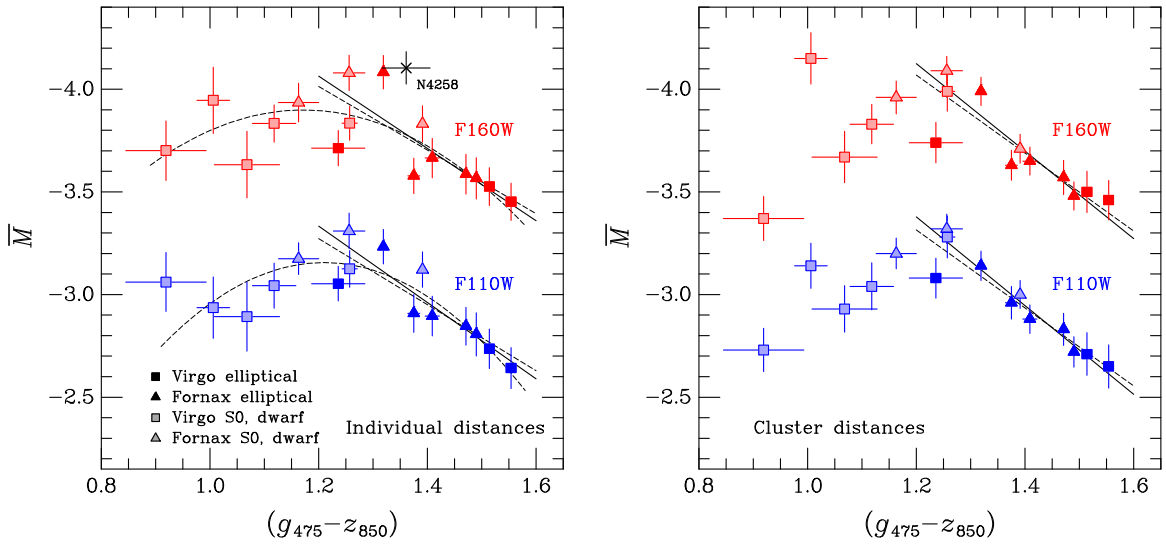


Figure 3. Fits to the absolute fluctuation magnitudes $\overline{M}$ as a function of $(g_{475}-z_{850})$ color. We also plot $\overline{M}$ for NGC 4258 for comparison. The calibration shown on the left is based on distances derived using the individual z-band SBF distances. The panel on the right shows the calibration using average cluster distances for Virgo and Fornax. Red points indicate H_{160} measurements (top set) and blue symbols are the J_{110} measurements (lower set). The dashed calibration lines show the quadratic fit and the linear calibration including IC 1919; the color of IC 1919 is intermediate between the other blue dwarf galaxies and the elliptical galaxies in our sample.

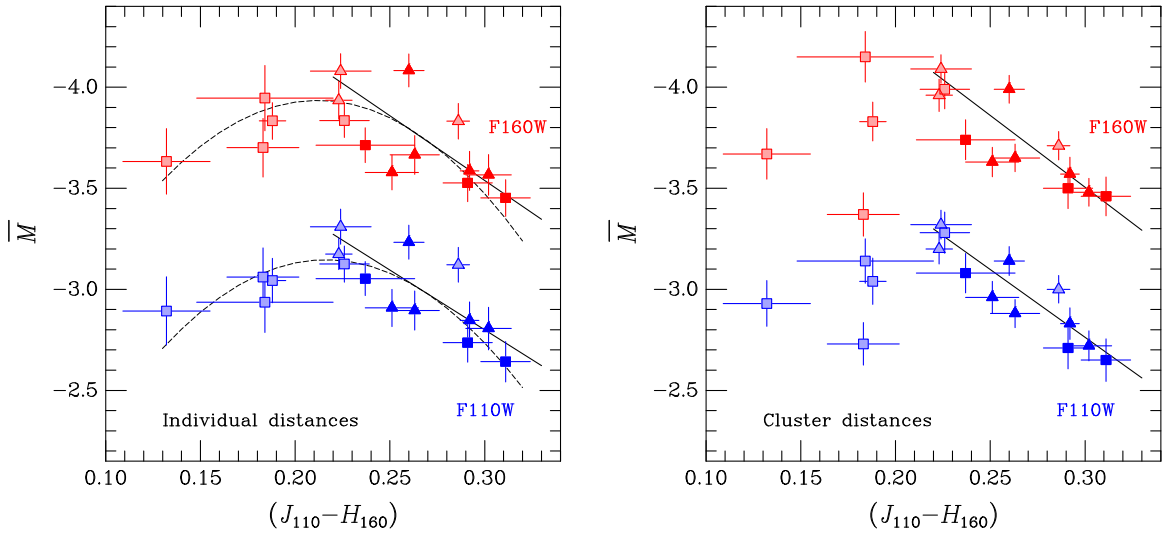


Figure 4. Fits to the absolute fluctuation magnitudes $\overline{M}$ as a function of $(J_{110}-H_{160})$ color derived using individual distances (left) and average cluster distances (right). Red symbols indicate H_{160} measurements (top set of points), and the lower set of blue points shows the J_{110} measurements. Symbol definitions are the same as in Figure 3.

4. ANALYSIS

4.1. Calibration of the WFC3/IR SBF Distance Scale

The SBF signal can be detected with *HST* in modest J_{110} and H_{160} exposures (an orbit or less) out to ~100 Mpc (e.g., Jensen et al. 2001). To take full advantage of WFC3/IR observations of early-type galaxies collected for a variety of purposes and measure accurate distances, we calibrated the WFC3/IR J_{110} and H_{160} SBF distances by fitting the absolute fluctuation magnitudes $\overline{M}$ as a function of both optical $(g_{475}-z_{850})$ and IR $(J_{110}-H_{160})$ colors. Determining the $\overline{M}$ values requires us to adopt a distance modulus $(m-M)$ for each galaxy. We used the z_{850} SBF distance moduli measured using ACS (Blakeslee et al. 2009). These measurements provide a consistent distance reference accurate to $\lesssim$0.08 mag for most of the galaxies, although the calibration becomes systematically less certain for $(g_{475}-z_{850}) < 1.05$ mag. We also adopted $(g_{475}-z_{850})$ values from the same ACS data, supplementing the published values from Blakeslee et al. (2009) with updated color measurements made using the original images in annuli that matched our IR observations. The ACS colors and distance moduli used to calibrate the IR SBF distance scale are listed in Table 4. Extinction-corrected $(J_{110}-H_{160})$ colors were measured using our WFC3/IR images.

As in optical bandpasses, the intrinsic luminosity of IR fluctuations varies with galaxy color. The SBF amplitude is sensitive to the brightness of the most luminous stars in a population, and bluer galaxies with a significant component of young or intermediate-age stellar populations have luminous AGB stars that enhance the SBF signal (e.g., Jensen et al. 2003). An accurate IR SBF distance calibration must take into account the brightening of fluctuations at intermediate and bluer colors. As in the previous F160W NICMOS

Table 6
Linear Calibration Coefficients

Calibration	a	b	χ^2/dof	rms	Distances	N_{gal}[a]
$\overline{M}_{110}$ versus $(g-z)$	−2.946 ± 0.015	2.16 ± 0.15	0.48	0.075	clust	11
$\overline{M}_{110}$ versus $(g-z)$	−2.935 ± 0.017	1.90 ± 0.16	0.86	0.086	clust	12
$\overline{M}_{110}$ versus $(g-z)$	−2.961 ± 0.032	1.86 ± 0.32	1.23	0.101	indiv	11
$\overline{M}_{110}$ versus $(g-z)$	−2.951 ± 0.034	1.61 ± 0.34	1.40	0.105	indiv	12
$\overline{M}_{110}$ versus $(J-H)$	−2.964 ± 0.032	6.7 ± 0.9	0.94	0.092	clust	12
$\overline{M}_{110}$ versus $(J-H)$	−2.977 ± 0.047	5.9 ± 1.4	1.76	0.130	indiv	12
$\overline{M}_{160}$ versus $(g-z)$	−3.699 ± 0.028	2.13 ± 0.27	1.35	0.114	clust	11
$\overline{M}_{160}$ versus $(g-z)$	−3.689 ± 0.029	1.90 ± 0.28	1.59	0.114	clust	12
$\overline{M}_{160}$ versus $(g-z)$	−3.712 ± 0.042	1.76 ± 0.42	2.49	0.138	indiv	11
$\overline{M}_{160}$ versus $(g-z)$	−3.704 ± 0.043	1.55 ± 0.44	2.45	0.134	indiv	12
$\overline{M}_{160}$ versus $(J-H)$	−3.718 ± 0.035	7.1 ± 1.1	1.35	0.121	clust	12
$\overline{M}_{160}$ versus $(J-H)$	−3.731 ± 0.050	6.4 ± 1.6	2.44	0.162	indiv	12

Notes. Linear fits for $(g_{475}-z_{850})>1.2$ or $(J_{110}-H_{160})>0.22$. For Vega magnitudes, subtract 0.7595 mag from WFC3/IR J_{110} and 1.2514 mag from H_{160} AB.
[a] IC 1919 was excluded from the $(g_{475}-z_{850})$ calibration because $(g_{475}-z_{850})<1.2$. The $(J_{110}-H_{160})$ color for IC 1919 is greater than 0.22, so it was included in the $(J_{110}-H_{160})$ calibration. We have included $(g_{475}-z_{850})$ calibrations with and without IC 1919 to show the relatively small influence this one galaxy has on the $(g_{475}-z_{850})$ calibration. The recommended calibration in Equations (3) and (4) exclude IC 1919.

Table 7
Quadratic Calibration Coefficients

Calibration	a	b	c	χ^2/dof	rms (mag)	Distances
$\overline{M}_{110}$ versus $(g-z)$	−2.991 ± 0.004	1.73 ± 0.025	4.55 ± 0.12	1.11	0.115	indiv
$\overline{M}_{110}$ versus $(J-H)$	−2.977 ± 0.011	6.3 ± 0.4	59 ± 6	1.06	0.129	indiv
$\overline{M}_{160}$ versus $(g-z)$	−3.723 ± 0.003	1.54 ± 0.022	3.38 ± 0.09	2.17	0.128	indiv
$\overline{M}_{160}$ versus $(J-H)$	−3.733 ± 0.030	6.9 ± 0.9	59 ± 15	1.74	0.149	indiv

Note. Quadratic fits for all 16 galaxies. Use only when necessary for $(g_{475}-z_{850}) < 1.2$ or $(J_{110}-H_{160}) < 0.22$.

calibration (Jensen et al. 2003), a linear fit to the red end of the sample was found to best represent the SBF calibration for distance measurements of typical giant elliptical galaxies. To determine the best slope of $\overline{M}$ as a function of galaxy color (see Figures 3 and 4), we adopted an iterative procedure that takes into account the uncertainties in both the $\overline{M}$ and color axes. We started by making an initial approximate fit ignoring the color uncertainties (i.e., using a standard least-squares approach). We computed the error ellipse for each point and the distance from the fitted line in units of the combined x and y uncertainties. Because the z_{850} SBF distances are also a function of $(g_{475}-z_{850})$, there is a small correlation between the x and y-axis uncertainties when fitting the individual-distance $\overline{M}$ values versus $(g_{475}-z_{850})$. We included the rotation of the error ellipse for that subset of the calibration fits. We then iteratively adjusted the fit coefficients to minimize the combined difference between the line and the data points, and then computed the rms in $\overline{M}$. This procedure was repeated for each of the filters for both $(g_{475}-z_{850})$ and $(J_{110}-H_{160})$, and for the two sets of $\overline{M}$ values derived from individual and common cluster distances. The coefficients and rms scatter for each fit are listed in Tables 6 and 7.

The intrinsic scatter in the optical SBF distance measurements is comparable to the Virgo and Fornax cluster depths as estimated by Blakeslee et al. (2009) (0.053 mag for Fornax, 0.085 mag for Virgo). Depending upon the location of the galaxy within the cluster, the error in the estimated distance may be larger when adopting the cluster mean or when using the individual galaxy distance. If the typical distance measurement error (including intrinsic scatter about the stellar population calibration) is less than the magnitude of the scatter from cluster depth, then it makes sense to calibrate the IR measurements using individual optical SBF distances. If the optical SBF distance measurement errors dominate, then it would be better to average all the optical SBF measurements and use a common cluster distance to calibrate the IR measurements. In the case of Fornax, the individual distance errors are larger than the scatter from cluster depth; the situation is less clear in Virgo, especially for the bluer galaxies. Table 6 presents calibrations computed using both individual distance moduli and average cluster distances of 31.09 and 31.51 mag for Virgo and Fornax, respectively (Blakeslee et al. 2009). The linear calibrations using cluster distances are not significantly different, particularly for the bright ellipticals located near the centers of the clusters, but the rms scatter is somewhat lower using the cluster distances.

The downturn in absolute SBF magnitude at the blue end is dominated by the four dwarf galaxies in Virgo. The four bluest galaxies have the largest color uncertainties and ranges, the lowest SBF S/N ratios, the lowest galaxy brightness compared to the sky, and the largest radial gradients in fluctuation amplitude. They also show evidence of a wide range in stellar population age and metallicity, as manifested in their large radial color and fluctuation magnitude gradients (the error bars shown in Figures 3 and 4 are larger than the measurement

errors and include the range of values due to radial gradients as described below in Section 5.5). These four Virgo galaxies were excluded from the linear calibration fits; IC 1919 was excluded from the $(g_{475}-z_{850})$ fits as well. Because the fluctuation amplitude is significantly lower in the bluest galaxies in this sample, we also present an alternative second order polynomial distance calibration fit that can be used for lower accuracy distance measurements of bluer galaxies (Figures 3 and 4). The quadratic fits were computed using the same iterative procedure that was used to make the linear fits, as described above. Higher-order fits are not justified given the sample size, measurement uncertainties, and large population variations between blue dwarf elliptical galaxies. The linear calibration is not useful for the bluer galaxies; they have too much population variation for SBF to be generally useful as a distance indicator. The quadratic calibration may be used to get approximate distances for bluer galaxies when necessary.

Calibration coefficients are shown in Tables 6 and 7. The coefficients are defined as follows:

$$\overline{M} = a + b[(g - z) - 1.4] + c[(g - z) - 1.4]^2, \quad (1)$$

$$\overline{M} = a + b[(J - H) - 0.27] + c[(J - H) - 0.27]^2, \quad (2)$$

where $c = 0$ for the linear fits.

For $(g_{475}-z_{850}) > 1.2$, researchers measuring distances should use the appropriate linear calibrations centered at the mean galaxy color as follows:

$$\overline{M}_{110} = (-2.946 \pm 0.015) + (2.16 \pm 0.15) \times [(g - z) - 1.4], \quad (3)$$

$$\overline{M}_{160} = (-3.699 \pm 0.028) + (2.13 \pm 0.27) \times [(g - z) - 1.4]. \quad (4)$$

The quadratic fits may be used for bluer galaxies, bearing in mind that the intrinsic scatter between blue galaxies is large. Quadratic fits are not shown for $\overline{M}$ computed using cluster distances because two of the bluest Virgo galaxies have individual optical SBF distance moduli that differ from the mean cluster modulus for Virgo by –0.20 and +0.33 mag (IC 3032 and IC 3025, respectively). The differences are 2.4 and 3.9 times larger than the Virgo cluster depth of 0.085 mag (Blakeslee et al. 2009); these galaxies are *probably* outside the Virgo cluster core and should not be included in a calibration based on mean cluster distances.

If $(g_{475}-z_{850})$ colors are not available, distances may be computed using the $(J_{110}-H_{160})$ color instead. The scatter in the calibration with $(J_{110}-H_{160})$ is larger than with $(g_{475}-z_{850})$ because the color range spanned is much smaller. For $(J_{110}-H_{160}) > 0.2$, the following relations centered at the mean galaxy color should be used:

$$\overline{M}_{110} = (-2.964 \pm 0.032) + (6.7 \pm 0.9)[(J - H) - 0.27], \quad (5)$$

$$\overline{M}_{160} = (-3.718 \pm 0.035) + (7.1 \pm 1.1)[(J - H) - 0.27]. \quad (6)$$

For magnitudes on the Vega system, subtract 0.7595 mag from J_{110} AB and 1.2514 mag from H_{160} AB for the WFC3/IR filters. The $(J_{110}-H_{160})$ color can be shifted to the Vega system by adding 0.4919 mag.

The results of our calibration analysis show that IR SBF measurements, especially in F110W, can produce high-accuracy distance measurements for red early-type galaxies with $(g_{475}-z_{850}) > 1.2$ and $(J_{110}-H_{160}) > 0.2$ mag using Equations (3) through (6). It is worth emphasizing again that the linear calibrations should not be extended to bluer colors: the bluer galaxies, comprising dwarf ellipticals and low-mass S0s, clearly do not follow extrapolations of the linear relations in Equations (3) through (6). Such blue galaxies likely have a wider variety of stellar populations than the giant ellipticals and S0 galaxies, and thus exhibit larger scatter, even with respect to the quadratic fits; they are not well-suited for highly accurate distance measurements. The stellar population implications are discussed in detail below in Section 5.

4.2. Independent Checks of the IR SBF Calibration Zero Point

Now, as for several decades, the forefront of progress in the measurement of extragalactic distances is limited primarily by the uncertainty in the calibration zero point (e.g., Freedman & Madore 2010; Riess et al. 2011). We have chosen to calibrate the WFC3 IR SBF distance scale using the extensive Virgo and Fornax optical SBF measurements made by Blakeslee et al. (2009) and their collaborators. This guarantees that the IR observational uncertainties and population variations will dominate the calibration uncertainty, not the precision of the reference distances. It does not, however, reduce the systematic zero point uncertainty present in the optical SBF measurements, which in turn were based on *HST* Cepheid distances (Freedman et al. 2001). Blakeslee et al. (2010) discuss in detail the small offsets between several of the largest SBF surveys, including Tonry et al. (2001) and Jensen et al. (2003), and the application of metallicity corrections to the *HST* Cepheid distance scale of Freedman et al. (2001). The systematic uncertainty in the SBF distance scale due to the uncertainty in the Cepheid zero point is about 0.1 mag (Blakeslee et al. 2010; Freedman & Madore 2010).

One approach for avoiding the Cepheid zero point uncertainty would be to use theoretical stellar population model predictions to calibrate the absolute $\overline{M}$ in galaxies of varying ages, metallicities, and colors. This model-based approach would therefore make the SBF a primary distance indicator independent of all other distance measurements, dependent only on our understanding of the luminosities and colors of red giants and other evolved stars of a particular age and metallicity. Comparisons with several different stellar population models are presented below in Section 5. As will be shown, infrared stellar population models are not sufficiently consistent to provide a robust zero point for distance calibration at the 10% level. At present, we find that observed IR SBF magnitudes are more useful for constraining stellar population models than the models are for constraining the SBF distance calibration in the IR.

Another approach is to find other distance indicators that are independent of the Cepheid calibration, such as the geometrical distance to NGC 4258. Water masers orbiting the central black hole in NGC 4258 have now been used to accurately determine the distance to this galaxy using a purely geometrical technique based on the Keplerian orbits of the masers (Humphreys et al. 2013). While SBF magnitudes are best measured in early-type galaxies, archival H_{160} images of the central bulge of NGC 4258 (GO-11570) provided us with an opportunity to explore the SBF calibration independent of the Cepheid distance scale. Given that an SBF measurement to NGC 4258 could allow us to bypass the systematic uncertainty in the Cepheid calibration, we felt it was worth an attempt. Unfortunately, the presence of clumpy dust and recent star formation prevented us from achieving an accurate calibration using this galaxy, even when optical color images were used to identify dusty regions. The

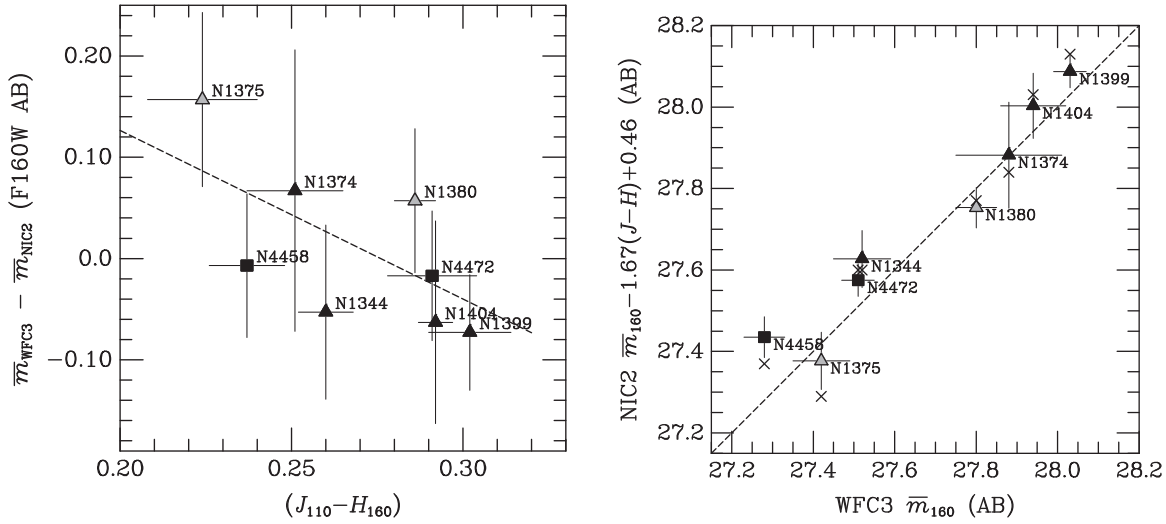


Figure 5. Comparison of NICMOS NIC2 and WFC3/IR H_{160} SBF measurements. The left panel shows the fit to the color term used to correct the points in the right panel, which shows the corrected NIC2 SBF magnitudes plotted as a function of the WFC3/IR SBF magnitudes. For reference, the SBF magnitudes with no color correction are shown with × symbols.

maser-calibrated fluctuation magnitude is significantly brighter (by ∼0.3 mag) than the calibration determined above for the elliptical and S0 galaxies in the Fornax and Virgo clusters with similar ($g_{475}-z_{850}$) colors (see Figure 3). This result was not a surprise; patchy dust adds to the fluctuation signal, as does the presence of younger populations containing bright AGB stars. Unfortunately, the geometrical distance to NGC 4258 does not provide a useful direct calibration of the SBF technique for elliptical galaxies. Given that optical Cepheid distances to NGC 4258 have now been published by Macri et al. (2006), Fausnaugh et al. (2015), and Hoffmann & Macri (2015), the future value of NGC 4258 in calibrating IR SBF is therefore most likely to be through an improved calibration of the Cepheid distance scale zero point and metallicity corrections.

Type Ia supernovae are one of the most accurate and widely-used distance measurement techniques in use today. In a recent paper, Cantiello et al. (2013) reported WFC3 J_{110} and H_{160} measurements of the SBF distance to NGC 1316, a Type Ia supernovae host galaxy in the Fornax cluster. They used the Jensen et al. (2003) F160W SBF calibration for NICMOS (including a metallicity correction to the Freedman et al. 2001 Cepheid zero point) and applied a 0.2 mag offset to the NICMOS zero point to account for the difference in filter width between NICMOS and WFC3/IR, based on predictions of the SPoT stellar population models (Raimondo et al. 2005; Raimondo 2009). To avoid uncertainties arising from differences between the methods used by Cantiello et al. and those used herein, we repeated the SBF analysis for NGC 1316 using the original WFC3/IR data (GO-11691) and the procedures described above. Our measured SBF magnitudes are listed in Tables 2 and 3; they are consistent with the Cantiello et al. (2013) values within the stated uncertainties. This galaxy is not an ideal SBF candidate due to the presence of extensive patchy dust near the center, but the regions farther out from the center appear relatively clean and the SBF signal is very strong. If we adopt the Blakeslee et al. (2009) z-band SBF distance (Table 4), the $\overline{M}$ values we find for NGC 1316 are brighter than the calibration prediction by ∼0.3–0.5 mag. The Tonry et al. (2001) ground-based I-band SBF measurement of 31.66 ±0.17 supports the Blakeslee et al. (2009) distance for NGC 1316. If NGC 1316 is located at the same distance as the core ellipticals in Fornax, then it appears to have a significant population of younger AGB stars, most likely the result of star formation that took place during a major merging episode a few Gyr ago, that biases the IR SBF magnitude. It may also have additional undetected dust contributing to the fluctuations. On the other hand, the IR and optical SBF distances are inconsistent with the published Sne I distances, which place NGC 1316 ∼0.25 mag closer than the Fornax cluster core. If we adopt the Ia supernova distance modulus for the three normal supernovae published by Stritzinger et al. (2010) of 31.248 ± 0.034 ± 0.04 instead of the z-band SBF distance, our IR SBF measurements would be much more consistent with the elliptical galaxy calibration. Additional work is needed to reconcile the SBF and supernova distances to this galaxy.

The IR SBF measurements of the maser host galaxy NGC 4258 and the supernova host galaxy NGC 1316 are not sufficiently accurate at present to reduce the systematic uncertainty in the IR SBF distance scale calibration to less than the 10% that we currently inherit from the Cepheid calibration of the optical SBF distances used for this study (Blakeslee et al. 2009, 2010). These galaxies have significant patchy dust and recent star formation, both of which enhance the IR SBF signal over what is typically observed in quiescent elliptical galaxies.

4.3. Comparison of WFC3 and NICMOS SBF Magnitudes

Eight galaxies in our current sample, mostly in the Fornax cluster, were included in the NICMOS NIC2 calibration of $\overline{M}_{160}$ (Jensen et al. 2003). A comparison of the SBF magnitudes is shown in Figure 5. To make the comparison using AB magnitudes, we added 1.313 mag to the published NIC2 SBF magnitudes to shift from the Vega magnitude system used by Jensen et al. (2003) to the AB mag system.[9]

The difference between NIC2 and WFC3/IR F160W SBF magnitudes shows a modest color dependence (left panel in

[9] http://www.stsci.edu/hst/nicmos/documents/handbooks/DataHandbookv8/nic_ch5.9.3.html

Figure 5). We fitted the slope (the color term in the conversion of NIC2 SBF magnitudes to WFC3/IR) including uncertainties in both $(J_{110}-H_{160})$ color and $\overline{m}_{160}$ SBF magnitudes; the rms for the fit is 0.055 mag and the χ^2 per degree of freedom is 0.66. The right panel of Figure 5 compares the NIC2 F160W apparent SBF magnitudes to WFC3/IR, with and without the color correction. The dashed line in the right panel of Figure 5 is not a fit, but shows the 45° perfect correlation line. SBF $\overline{m}_{160}$ measurements made using NIC2 prior to the installation of the NICMOS cryocoolers may be compared to WFC3/IR measurements using the relation

$$\overline{m}_{160} = \overline{m}_{160,\mathrm{NIC2}} - 1.67\left(J_{110}-H_{160}\right) + 0.46 \qquad (7)$$

(all AB magnitudes). Because we are comparing apparent fluctuation magnitudes directly, we do not need to be concerned about differences in distance scale calibrations between the two studies or cameras.

5. STELLAR POPULATION MODELS

We turn now to how IR SBF measurements, with their sensitivity to red giant branch and intermediate-age AGB stars, can expose interesting differences between galaxies with different star formation histories and better constrain single-burst stellar population models.

The brightening of the SBF magnitudes in elliptical and S0 galaxies at intermediate colors seen in the centers of Figures 3 and 4, and the subsequent drop in SBF brightness in the bluest dwarf ellipticals in this sample, provide powerful new constraints for stellar population models, which have only been compared to redder galaxies in previous near-IR SBF studies. The scatter among the bluest galaxies in our sample is much larger than the observational uncertainties, and many of these galaxies exhibit significant radial gradients in IR fluctuation magnitude, color, or both. The current sample includes bluer and fainter galaxies than are typically targeted for SBF distance measurements, and the breaking of the age-metallicity degeneracy in near-IR fluctuations provides a unique opportunity to explore the stellar populations in these galaxies.

Single-burst stellar population (often abbreviated SSP) models with constant age and metallicity are frequently used to interpret broad band colors and other properties of unresolved stellar populations in distant galaxies, including SBF magnitudes. These models are usually calculated by integrating collections of properly weighted isochrones, and can be used to compute predicted SBF magnitudes directly without any need to link the apparent SBF magnitudes to an external distance scale calibration. Examples of theoretical SBF comparisons include Worthey (1993, 1994), Liu et al. (2000, 2002), Blakeslee et al. (2001), Cantiello et al. (2003), Raimondo et al. (2005), Marín-Franch & Aparicio (2006), Biscardi et al. (2008), and Lee et al. (2010).

We compared our SBF measurements to three recent sets of SSP models for which J_{110} and H_{160} SBF magnitudes have been computed. The purpose of these comparisons is to explore the limitations of our SBF distance calibration and provide input to researchers working to improve stellar population models, particularly for understanding galaxy evolution, when the observations may not so easily distinguish the effects of age and metallicity as our near-IR SBF measurements do. While we compared our IR SBF measurements to single-burst population models, real galaxies are composed of composite stellar populations with potentially many bursts of star formation. Because the fluctuations are dominated by the most luminous stars weighted as L^2, they are even more strongly weighted toward young, luminous populations than are broad-band galaxy colors (Tonry & Schneider 1988). A composite population model will therefore predict an SBF magnitude close to that of the younger (or brighter) model component, even when the young population is only a small fraction (∼10% to 20%) of the galaxy by mass (Blakeslee et al. 2001; Liu et al. 2002; Jensen et al. 2003). The comparison to SSP model ages shown in this section should be considered the time since the most recent episode of star formation, not the average age of the dominant stellar population by mass.

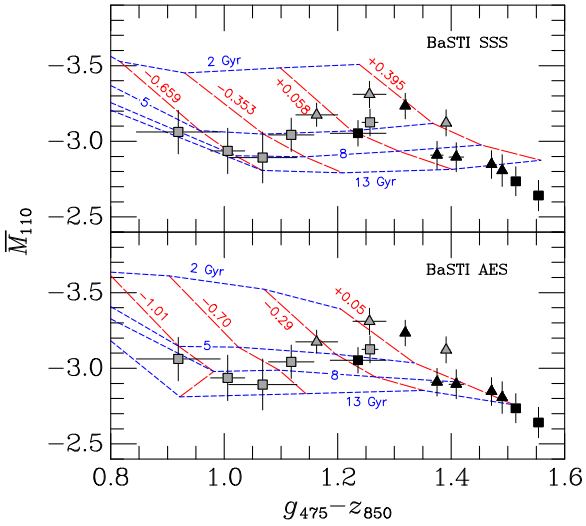


Figure 6. Teramo BaSTI models compared to $\overline{M}_{110}$ as a function of galaxy $(g_{475}-z_{850})$ color for two metallicity variants of the models computed using the individual galaxy distances: the "SSS" models (top panel) are solar-scaled abundances spanning the range from [Fe/H] = −0.659 to +0.395. The "AES" models (lower panel) have enhanced α element compositions and reduced [Fe/H] to make the overall metallicity Z the same as the solar-scaled models shown in the top panel. The range of [Fe/H] spanned by the AES models is −1.01 to +0.05. Lines of constant metallicity are shown with red dashed lines, and lines of constant age from 2 to 13 Gyr are plotted with dotted blue lines.

5.1. Teramo BaSTI Models

The first set of stellar population models we consider here are based on the Teramo BaSTI models[10] using a standard Salpeter initial mass function with a low-mass cutoff of 0.5 $M_\odot$ (Pietrinferni et al. 2004, 2006; Cordier et al. 2007; Lee et al. 2010). We compared our observed fluctuation magnitudes $\overline{M}_{110}$ to absolute fluctuation magnitudes computed for two variants of the BaSTI models: the solar-scaled abundance ratio models without convective overshoot, and the α-enhanced version of the models described by Lee et al. (2010). The latter models have a mean [α/Fe] of ∼0.4 dex, but with physically-motivated variations in the abundance ratios of the individual α elements (i.e., O, Mg, Si, S, Ca, Ti); the [Fe/H] abundances in these models have been correspondingly reduced to keep a fixed [Z/H].

The solar-scaled models shown in the top panel of Figure 6 do not match the reddest giant ellipticals as well as the α-enhanced models shown in the lower panel (the

[10] http://193.204.1.62/index.html

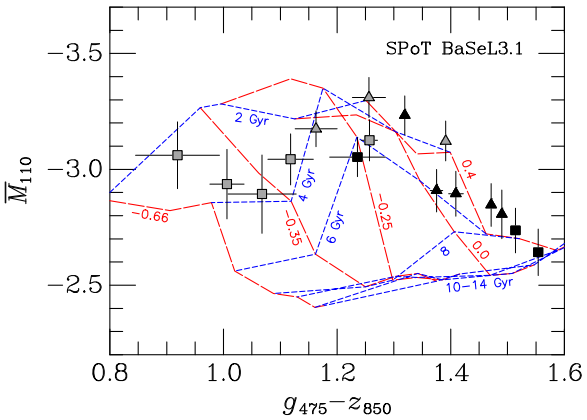


Figure 7. Recent versions of the Teramo SPoT models compared to $\overline{M}_{110}$ measurements as in Figure 6. The metallicity range for these models spans [Fe/H] = −0.66 to +0.4 and the ages span from 2 to 14 Gyr. The lines and symbols are defined in the same way as in Figures 3 and 6.

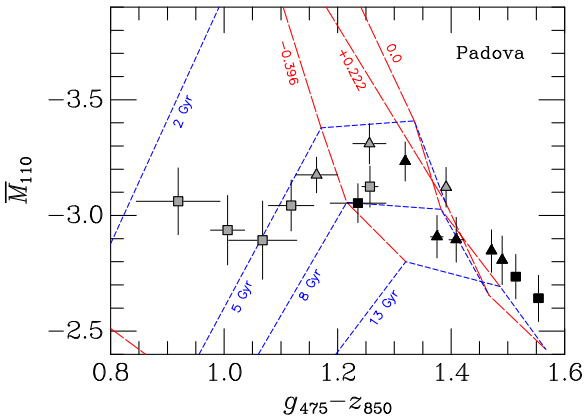


Figure 8. Stellar population models based on the Padova isochrones compared to $\overline{M}_{110}$ measurements computed using individual SBF distances. The symbol definitions are the same as in Figure 3. Lines of constant metallicity from [Fe/H] = −0.705 (in the extreme lower left corner) to 0.0 and +0.222 (overlapping at right) are shown with red dashed lines. Lines of constant age from 2 to 13 Gyr are plotted with dotted blue lines.

solar-scaled models are included here to provide a point of reference with past SBF-model comparisons that only used solar-scaled metallicity models). Both model variations suggest that the intermediate-color galaxies in our sample have younger populations, as expected due to the presence of intermediate-age AGB stars. The models imply that the bluest galaxies are old and metal-poor. While we have chosen to show the comparison for $\overline{M}_{110}$ and $(g_{475}-z_{850})$, the conclusions are the same when we compare the models to $\overline{M}_{160}$ instead of $\overline{M}_{110}$ or $(J_{110}-H_{160})$ instead of $(g_{475}-z_{850})$.

5.2. Teramo SPoT Models

The second set of models was developed by the Teramo SPoT group (version BaSeL3.1, Raimondo et al. 2005; Raimondo 2009). The Teramo SPoT models pay special attention to the thermally pulsating asymptotic giant branch (TP-AGB) stars, particularly in young to intermediate-age populations. The SPoT model SBF magnitude predictions in the near-IR have been empirically compared to a variety of clusters in the Large Magellanic Cloud and have been shown to match empirical measurements of SBF magnitudes, integrated magnitudes, star counts, and colors (Cantiello et al. 2007; Raimondo 2009; Cantiello 2012).

The SPoT models in Figure 7 differ significantly from the BaSTI models in Figure 6, although they are based on the same stellar evolutionary tracks as the BaSTI models in the upper panel of Figure 6. The SPoT models derive SBF magnitudes in a procedure that allows modelers to statistically combine various stellar population models produced by stochastic variations in the number and properties of bright and rare stars, including the TP-AGB and horizontal branch populations in intermediate-age and old stellar populations. Overall, the SPoT and BaSTI models agree for the red and intermediate-color ellipticals, with somewhat fainter SBF magnitudes for the oldest and most metal-rich giant ellipticals. The SPoT models predict a larger spread in SBF magnitude at younger ages and imply that the bluer galaxies in the sample are all younger than about 5 Gyr, in contrast with the BaSTI models, which span a narrower range in $\overline{M}_{110}$ and imply ages greater than 5 Gyr for the bluest galaxies.

5.3. Padova Models

The third set of models is based on the Padova isochrones (Figure 8), which include sophisticated handling of the TP-AGB evolutionary phase. The Padova tracks use solar-scaled metallicity abundance ratios and do not include α-element enhancement. SBF magnitudes were computed by Lee et al. (2010) using the evolutionary tracks of Marigo et al. (2008).

The Padova SSP models show the largest spread in $\overline{M}_{110}$ of all the models considered here. At the red end, the giant ellipticals again agree with old, metal-rich population models, with the intermediate bluer galaxies having brighter fluctuations and younger populations. The bluest galaxies in the sample are consistent with ages intermediate between the BaSTI and SPoT models, in the range 3–7 Gyr. Because of their larger spread in SBF magnitude predictions, the Padova models, as compared to the other sets of models, suggest that the data provide better discrimination between ages and metallicities.

5.4. Fluctuation Colors

SBF measurements at two wavelengths can be used to eliminate uncertainties resulting from distance error; for instance, the "fluctuation color" $(\overline{m}_{110}-\overline{m}_{160})$ can be compared to stellar population models in a distance-independent way. Figure 9 compares $(\overline{m}_{110}-\overline{m}_{160})$ to the Teramo BaSTI solar-scaled and α-enhanced models as a function of $(g_{475}-z_{850})$. As discussed by Lee et al. (2010), the predicted SBF magnitudes are sensitive to α-element abundance mostly because of the effects of oxygen-enhancement on the upper red giant branch and AGB phase. The data in Figure 9 agree on average with the α-enhanced models relatively well, but only poorly with the solar-scaled models. However, this set of α-enhanced models also predicts a narrower range of $(\overline{m}_{110}-\overline{m}_{160})$ than is observed. In particular, the low-mass dwarf IC 3032 in Virgo agrees better with the locus of the solar-scaled models; this may indicate real variation in α-element abundance ratios among the sample galaxies. We conclude that fluctuation colors can provide useful information on elemental abundance ratio trends with age and metallicity in elliptical galaxies, independent of the uncertainties in the distance calibration. In addition,

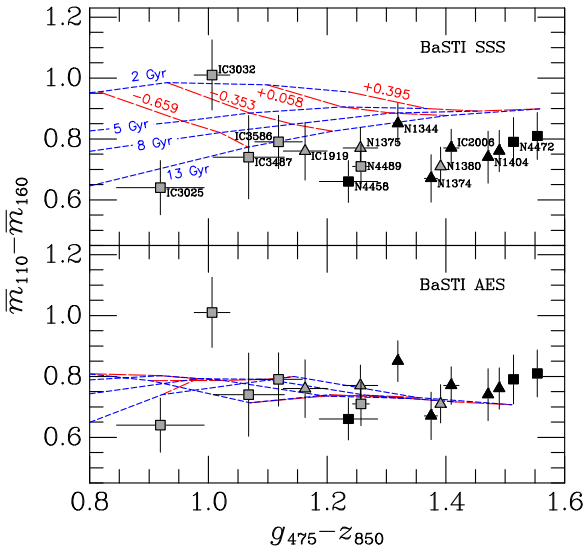


Figure 9. Distance-independent IR fluctuation colors for the solar-scaled and α-enhanced Teramo models. Blue dotted lines indicate lines of constant age, from 2 to 13 Gyr. Red dashed lines show constant metallicity tracks, from [Fe/H] = −0.659 at the left to +0.395 at right (upper panel) and [Fe/H] = −1.01 to +0.05 (lower panel). The two points that are not labeled for clarity are NGC 1399 in Fornax and NGC 4636 in Virgo. Symbol definitions are the same as in Figures 3 and 6.

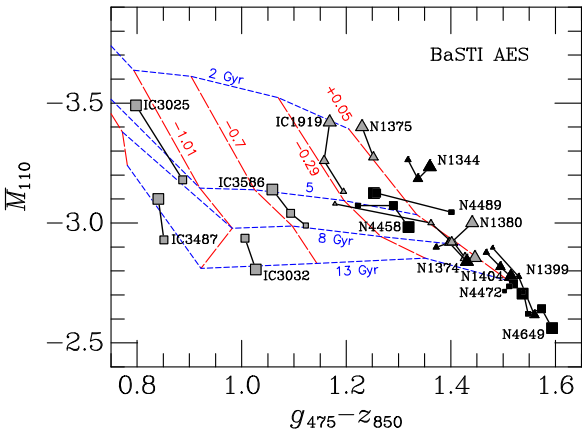


Figure 10. Radial SBF and color gradients for the survey galaxies, with larger symbols corresponding to the inner annuli in which SBFs were measured and smaller symbols being outer regions. Black lines link measurements in the same galaxy. The measurements are compared to the BaSTI α-enhanced models; the conclusions are the same for the other models because they all have lines of constant metallicity with similar slopes for this color range. IC 2006 is not labeled but falls very close to NGC 1374.

comparisons with other observables that are sensitive to age, metallicity, or α-enhancement should provide powerful joint constraints for future stellar population models.

5.5. Radial SBF Gradients

To further explore the origins of the scatter in SBF magnitude among the low-luminosity blue dwarf ellipticals, we measured the radial behavior of the SBF amplitude. Many of the galaxies in our sample, particularly the low-luminosity galaxies, are quite elliptical. To get the cleanest gradient measurements possible, we repeated the SBF analysis and measured $(g_{475}-z_{850})$ colors in elliptical annuli for a subset of the galaxies with significant $\overline{M}$ gradients (IC 1919, NGC 1375, NGC 1380, IC 3025, IC 3487, and IC 3586; see Figure 1). For the rest of the sample we used the circular annulus SBF and $(g_{475}-z_{850})$ color measurements previously used for the calibration. The results are plotted in Figure 10.

The comparison of radial SBF gradients to the models shows a significant difference between the giant ellipticals and the smaller galaxies. Most of the galaxies show a gradient sloping from upper left to lower right in Figure 10, roughly along lines of constant metallicity. While the various models look quite different in detail, they all have lines of constant metallicity sloping in approximately the same direction at the relevant colors. The lower-luminosity galaxies have centers (larger symbols in Figure 10) consistent with younger stellar populations (brighter fluctuations) and nearly constant metallicities: IC 1919, IC 3025, IC 3487, IC 3586, and NGC 1375 all have brighter fluctuations near their centers. In contrast, the giant ellipticals on the red end of the diagram tend to show older and sometimes more metal-rich populations in their centers: IC 3032, IC 2006, NGC 1374, NGC 1399, NGC 1404, NGC 4458, and NGC 4649 have fainter fluctuations toward their centers. Four of the sixteen galaxies (NGC 1380, NGC 1344, NGC 4458, and NGC 4472) appear to have color and SBF gradients consistent with little or no age variation. The majority of the galaxies show gradients consistent with primarily age variations, however.

The IR SBF and color gradients hint at differing formation histories for the galaxies. As noted above, low-luminosity blue elliptical galaxies usually have older populations at large radii, and thus to have formed stars more recently near their centers from metal-poor gas, while the giant ellipticals formed stars in their cores long ago from enriched gas. Optical studies of SBF gradients, in contrast, suggest that the outer parts of giant ellipticals have colors and fluctuation magnitudes consistent with lower metallicity populations and little or no age gradient (Cantiello et al. 2005, 2007). Our IR measurements do not cover as large a range in radius as the optical studies because of the smaller field of view spanned by the IR detectors and the brighter sky background. Because the data here are confined within the effective radius of the several largest galaxies (Table 1), we cannot derive strong constraints on the large-scale stellar population gradients in these giant galaxies. Interestingly, the physical size ($r \lesssim 5$ kpc) of the radial region probed by our SBF data is similar to that of the luminous dense cores observed at high redshift (e.g., van Dokkum et al. 2010; van der Wel et al. 2014; Fritz et al. 2014), which are believed to be the seeds around which massive modern-day ellipticals were assembled through hierarchical merging and accretion. Our results on the old ages and relative homogeneity of the stellar populations of the giant ellipticals within the central region are thus in line with this scenario for early-type galaxy evolution, if the elliptical galaxies in our sample may be compared with the high-redshift counterparts. At much larger radii in giant ellipticals, evidence exists from optical and IR color gradients that the stellar populations at several effective radii are older than the mean stellar age in the core (La Barbera et al. 2012), but see also Greene et al. (2015) results for MASSIVE Survey (Ma et al. 2014) galaxies. While our data do not probe such large radii in the massive galaxies, we find the same trend for the lower mass galaxies where our measurements do reach beyond the effective radius. It would be interesting to extend the IR SBF gradients to correspondingly

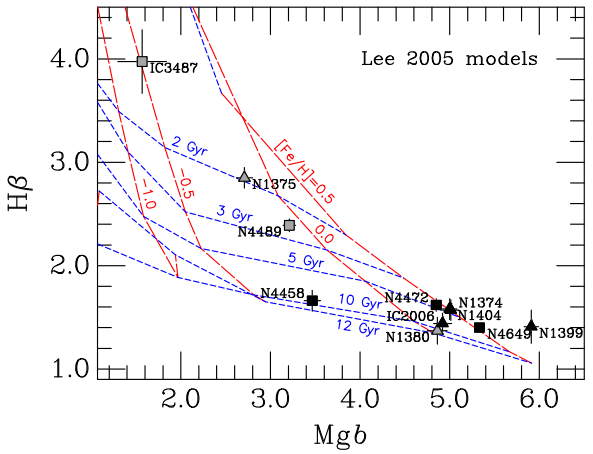


Figure 11. Lick index measurements for eleven of the galaxies in our sample (Kuntschner 2000; Trager et al. 2000; Caldwell et al. 2003) as compared with the α-enhanced models from Lee & Worthey (2005). Hβ is more age-sensitive, while Mg*b* is metallicity-sensitive. Such data provide an independent way of checking the SBF model comparison conclusions; see the text.

large radii in the massive ellipticals to see if these also show evidence for larger ages in the galaxy outskirts.

Crucial for the purpose of distance measurement, the radial and population variations in the reddest galaxies cause SBF magnitude variations *along* the direction of the linear calibration. These galaxies are ideally suited for distance measurement because variations from galaxy to galaxy in age or metallicity are adequately accommodated by the calibration slope with $(g_{475}-z_{850})$. On the other hand, the radial gradients in SBF magnitude in the bluer dwarf galaxies (the gray symbols in the left half of Figure 10 are perpendicular to the quadratic calibration relation, leading to *greater* scatter in the distance calibration. These low-luminosity dwarfs show a wide range of ages and metallicities, with several showing evidence of recent star formation near their centers, as revealed by their SBF magnitudes.

Only one set of SBF measurements and models is shown in Figure 10; the general conclusions, however, are consistent for all the models discussed herein. The radial variations are consistently sloped along lines of constant metallicity for all the models, so even though the models might not agree on the specific age and metallicity of a particular galaxy, the trend toward younger ages in the centers of bluer dwarf galaxies is consistent for all the models.

5.6. Line Index Age and Metallicity Constraints

Eleven of the galaxies in our sample have published $H\beta$ and Mg*b* Lick index measurements from Kuntschner (2000), Trager et al. (2000), and Caldwell et al. (2003). The former index is more sensitive to age, and the latter to metallicity. Figure 11 compares these data with the +0.3 dex α-enhanced model predictions from Lee & Worthey (2005). The line index measurements generally sample different regions of the galaxies than our SBF data, but we again see that the reddest ellipticals agree with the old, metal-rich population models. The youngest galaxies as determined using absorption lines, do not always agree with the SBF models. IC 3487 has the strongest Hβ index but the faintest $\overline{M}_{110}$ among the bluer galaxies, implying a relatively older age compared to NGC 1375, which has somewhat weaker Hβ and brighter $\overline{M}_{110}$ (although there is considerable variation between SBF models at the youngest ages). Further work is needed to explore the radial behavior of Mg*b* and Hβ as compared to our SBF measurements on the same scales, particularly since we detect a significant radial age gradient in many of the lower-luminosity galaxies.

5.7. Model Comparison Summary

The SBF models shown in Figures 6–8 agree for old, metal-rich populations such as those commonly found in giant elliptical galaxies, and for which extensive comparisons have been made in the past (e.g., Jensen et al. 2003; Cantiello 2012 Fritz 2012). At younger ages and lower metallicities, the three sets of models are significantly different, and the conclusions we draw about the ages of the blue dwarf ellipticals are strikingly different. These three sets of models allow for the blue, low-mass dwarf ellipticals to potentially have a range of ages from 2 to 14 Gyr, and [Fe/H] from about −1 to −0.3. Optical *I*-band SBF measurements of blue dwarf ellipticals (Mieske et al. 2006) also show a large spread of fluctuation magnitudes and younger implied ages. Since each set of models was computed with the aim of understanding something different—the role of α-enhancement in early-type galaxies for the BaSTI models (Lee et al. 2010) and the TP-AGB phase for the SPoT and Padova models (Cantiello et al. 2007; Raimondo 2009; Lee et al. 2010; Cantiello 2012)—the differences shown here provide the starting point for future detailed comparison of the near-IR properties of actual red giant and AGB stars in unresolved stellar populations with model predictions. We have chosen to show model comparisons using $\overline{M}_{110}$ plotted against $(g_{475}-z_{850})$ computed using the individual galaxy optical SBF distances. The general trends and conclusions are similar when the models are compared to $\overline{M}_{160}$ or plotted against $(J_{110}-H_{160})$.

It is beyond the scope of this study to provide a critical analysis of the strengths and shortcomings of each of these sets of models. For the purposes of this study, we conclude that the IR SBF distance calibration is robust when applied to old, red, metal-rich galaxies like the giant ellipticals typically found in environments like Virgo and Fornax, and even to some with intermediate-age populations and somewhat bluer colors. The bluer dwarf ellipticals, on the other hand, provide important new observational constraints that should be of interest to researchers constructing the next generation of stellar population models. It is clear that better constraints from data such as these will be valuable in better defining the properties of young, metal-poor populations, and the brightness of the TP-AGB stars within these populations.

6. RECOMMENDATIONS FOR MEASURING IR SBF DISTANCES WITH WFC3

WFC3 on the *HST* makes it possible to measure IR SBF magnitudes at relatively large distances in modest exposure times. Based on our experience with the Fornax and Virgo cluster calibration data presented here, as well as tests with WFC3/IR observations in the Coma cluster from *HST* program GO-11711 (see Blakeslee 2013) and with the instrument exposure time calculator, we provide the following guidelines to help other astronomers plan WFC3 SBF observations and make use of existing data in the *HST* archive.

1. The fluctuations are brighter at H_{160} than at J_{110}, but the J_{110} filter is signficantly wider than H_{160} (by 0.8 mag),

which largely cancels out the brightness advantage. The image quality is slightly better at J_{110} than H_{160}, and the background is slightly lower. The net effect is that exposure times to achieve a particular SBF S/N ratio are about the same in the two filters, but the ability to detect and remove contaminating point sources (primarily globular clusters) is better at J_{110}, and there is less scatter in the calibration. We therefore advise choosing J_{110} over H_{160} when possible. The broad F140W filter would be a good alternative, unhampered by the 1.083 μm He emission line in the upper atmosphere, but that bandpass remains uncalibrated for SBF.

2. Typical one-orbit exposure times ($\sim$2400 s) suffice for measuring distances in either J_{110} or H_{160} out to about 80 Mpc. This distance limit is imposed by the point source sensitivity required to detect and remove globular clusters from the image, with the goal of reaching within $\sim$1 mag of the peak of the globular cluster luminosity function in J_{110}, or $\sim$1.5 mag of the peak in H_{160}, for which the fluctuations are relatively brighter (Jensen et al. 1998). The SBF signal itself can be detected to much larger distances (beyond 100 Mpc) in a single orbit, but the large correction for contaminating point sources would then dominate the uncertainty.
3. Exposure times for more distant galaxies should be scaled to achieve a point source sensitivity sufficient to detect and remove globular clusters 1–1.5 mag brighter than the peak of the globular cluster luminosity function. The exposure time needed to detect the stochastic fluctuations that comprise the SBF signal goes as d^2, but the time required to detect the globular clusters increases significantly faster, scaling as d^3 to d^4, because of the bright background on which the globular clusters are superimposed.
4. To avoid issues with correlated noise, do not use the default *HST* pipeline-combined images. Use the *flt* files without correcting the WFC3/IR field distortion. It may be possible to recreate the *drz* files using the lanczos3 kernel in the *astrodrizzle* package; this approach was not tested for WFC3/IR as part of this study, but has been used successfully in the past for ACS data (see Cantiello et al. 2005; Mei et al. 2005a).
5. Because SBF magnitudes depend on the properties of the stellar populations, high-quality color data are essential to determine accurate distances. For the most accurate SBF distances, one should target giant elliptical and S0 galaxies with old stellar populations, for which $(g_{475}-z_{850})$ colors are greater than 1.2 or $(J_{110}-H_{160})$ are greater than 0.22 AB mag. The population variations at bluer colors are too great for robust distance measurements. If possible, it is best to use ACS $(g_{475}-z_{850})$ colors, but WFC3/IR $(J_{110}-H_{160})$ colors are an acceptable alternative. If necessary, other color indices may be translated to $(g_{475}-z_{850})$ or $(J_{110}-H_{160})$ using well-constrained empirical or model relations for old, metal-rich populations.

7. SUMMARY

We have measured J_{110} and H_{160} SBF magnitudes and $(J_{110}-H_{160})$ colors for 16 early-type galaxies in the Virgo and Fornax clusters observed with WFC3/IR. All of these galaxies have previously measured SBF distances and $(g_{475}-z_{850})$ colors from ACS. We find that the luminous red galaxies in the sample follow linear relations between absolute SBF magnitude and optical or IR color; SBF distances to such galaxies can be determined within a statistical uncertainty of 5% using the calibration relations that we have presented in Equations (3) through (6). The systematic uncertainty of this calibration is $\sim$10% due to the uncertainty in the Cepheid calibration on which this work is based. Stellar population models are not consistent enough to provide a direct calibration of the IR SBF technique accurate to 10%, but they are valuable for inferring age and metallicity trends in and among the sample galaxies. The scatter in SBF magnitude among bluer galaxies is large, indicating that a wider variety of stellar populations dominates the light from these galaxies and that a simple broadband color does not adequately parameterize the complexities inherent in such populations. Some galaxies, particularly those of intermediate color, clearly have younger (4–8 Gyr) populations, likely with AGB stars that enhance the IR fluctuation amplitude. Bluer galaxies, primarily dwarf ellipticals, may have very-low metallicities and/or younger ages, with the interpretations varying among different sets of stellar population models. Finally, we have provided practical advice to guide researchers interested in undertaking SBF measurements with WFC3/IR.

Based on observations made with the NASA/ESA *Hubble Space Telescope*, obtained at the Space Telescope Science Institute, which is operated by the Association of Universities for Research in Astronomy, Inc., under NASA contract NAS 5-26555. These observations are associated with program #11712. Additional data from program #11570 were obtained from the Data Archive. J. Jensen, Z. Gibson, and N. Boyer acknowledge the support of the Utah Valley University Scholarly Activities Committee. Z. Gibson was also supported by the Utah NASA Space Grant Consortium award NNX10AJ77H. M. Cantiello is grateful for support from the FSE-Abruzzo "Sapere e Crescita" project and the PRIN-INAF-2014 grant (P.I. Gisella Clementini). H.C. acknowledges support from the National Research Foundation of Korea to the Center for Galaxy Evolution Research. This research has made use of the NASA/IPAC Extragalactic Database (NED) which is operated by the Jet Propulsion Laboratory, California Institute of Technology, under contract with the National Aeronautics and Space Administration.

REFERENCES

Bennett, C. L., Larson, D., Weiland, J. L., et al. 2013, ApJS, 208, 20
Bertin, E., & Arnouts, S. 1996, A&AS, 117, 393
Binggeli, B., Sandage, A., & Tammann, G. A. 1985, AJ, 90, 1681
Biscardi, I., Raimondo, G., Cantiello, M., & Brocato, E. 2008, ApJ, 678, 168
Blake, C., Kazin, E. A., Beutler, F., et al. 2011, MNRAS, 418, 1707
Blakeslee, J. P. 2012, Ap&SS, 341, 179
Blakeslee, J. P. 2013, in IAU Symp. 289, ed. R. de Grijs (Cambridge: Cambridge Univ. Press), 304
Blakeslee, J. P., Cantiello, M., Mei, S., et al. 2010, ApJ, 724, 657
Blakeslee, J. P., Jordán, A., Mei, S., et al. 2009, ApJ, 694, 556
Blakeslee, J. P., Tonry, J. L., & Metzger, M. R. 1997, AJ, 114, 482
Blakeslee, J. P., Vazdekis, A., & Ajhar, E. A. 2001, MNRAS, 320, 193
Brammer, G., Pirzkal, N., McCullough, P., & MacKenty, J. 2014, Time-varying Excess Earth-glow Backgrounds in the WFC3/IR Channel, WFC3 Instrument Science Rep. 2014-03 (Baltimore, MD: STScI)
Caldwell, N., Rose, J. A., & Concannon, K. D. 2003, AJ, 125, 2891
Cantiello, M. 2012, Ap&SS, 341, 187

Cantiello, M., Blakeslee, J. P., Raimondo, G., et al. 2007, ApJ, 668, 130
Cantiello, M., Blakeslee, J. P., Raimondo, G., Mei, S., Brocato, E., & Capaccioli, M. 2005, ApJ, 634, 239
Cantiello, M., Grado, A., Blakeslee, J. P., et al. 2013, A&A, 552, 106
Cantiello, M., Raimondo, G., Brocato, E., & Capaccioli, M. 2003, AJ, 125, 2783
Chen, C.-W., Côté, P., West, A. A., Peng, E. W., & Ferrarese, L. 2010, ApJS, 191, 1
Cordier, D., Pietrinferni, A., Cassisi, S., & Salaris, M. 2007, AJ, 133, 468
Côté, P., Blakeslee, J. P., Ferrarese, L., et al. 2004, ApJS, 153, 223
Eisenstein, D. J., Zehavi, I., Hogg, D. W., et al. 2005, ApJ, 633, 560
Fausnaugh, M. M., Kochanek, C. S., Gerke, J. R., et al. 2015, MNRAS, 450, 3597
Ferguson, H. C. 1989, AJ, 98, 367
Ferrarese, L., Côté, P., Jordán, A., et al. 2006, ApJS, 164, 334
Ferrarese, L., Freedman, W. L., Hill, R. J., et al. 1996, ApJ, 464, 568
Ferrarese, L., Mould, J. R., Kennicutt, R. C., Jr., et al. 2000, ApJ, 529, 745
Freedman, W. L., & Madore, B. F. 2010, ARA&A, 48, 673
Freedman, W. L., Madore, B. F., Gibson, B. K., et al. 2001, ApJ, 553, 47
Freedman, W. L., Madore, B. F., Mould, J. R., et al. 1994, Natur, 371, 757
Freedman, W. L., Madore, B. F., Scowcroft, V., et al. 2012, ApJ, 758, 24
Fritz, A. 2012, PASA, 29, 489
Fritz, A., Scodeggio, M., & Ilbert, O. 2014, A&A, 563, 92
Frogel, J. A., Persson, S. E., Matthews, K., & Aaronson, M. 1978, ApJ, 220, 75
Gibson, B. K., Stetson, P. B., Freedman, W. L., et al. 2000, ApJ, 529, 723
Greene, J. E., Janish, R., Ma, C.-P., et al. 2015, ApJ, 807, 11
Greenhill, L. J., Jiang, D. R., Moran, J. M., et al. 1995, ApJ, 440, 619
Harris, W. E. 2001, in Star Clusters, Vol. 28, Saas-fee Advanced Courses, ed. L. Labhardt & B. Binggeli (Berlin: Springer), 223
Herrnstein, J. R., Moran, J. M., Greenhill, L. J., et al. 1999, Natur, 400, 539
Hoffmann, S. L., & Macri, L. M. 2015, AJ, 149, 183
Humphreys, E. M. L., Reid, M. J., Moran, J. M., Greenhill, L. J., & Argon, A. L. 2013, ApJ, 775, 13
Jensen, J. B., Luppino, G. A., & Tonry, J. L. 1996, ApJ, 468, 519
Jensen, J. B., Tonry, J. L., Barris, B. J., et al. 2003, ApJ, 583, 712
Jensen, J. B., Tonry, J. L., & Luppino, G. A. 1998, ApJ, 505, 111
Jensen, J. B., Tonry, J. L., Thompson, R. I., et al. 2001, ApJ, 550, 503
Jordán, A., Blakeslee, J. P., Côté, P., et al. 2007, ApJS, 169, 213
Kalirai, J. S., Cox, C., Dressel, L., et al. 2010, WFC3 Pixel Area Maps, WFC3 Instrument Science Rep. 2010-08 (Baltimore, MD: STScI)
Kelson, D. D., Illingworth, G. D., Freedman, W. F., et al. 1996, ApJ, 463, 26
Kormendy, J., & Ho, L. C. 2013, ARA&A, 51, 511
Krist, J. E., Hook, R. N., & Stoehr, F. 2011, Proc. SPIE, 8127, 81270J
Kuntschner, H. 2000, MNRAS, 315, 184
La Barbera, F., Ferreras, I., de Carvalho, R. R., et al. 2012, MNRAS, 426, 2300
Lee, H.-c., Worthy, G., & Blakeslee, J. P. 2010, ApJ, 710, 421
Lee, H.-c., & Worthey, G. 2005, ApJS, 160, 176
Liu, M. C., Charlot, S., & Graham, J. R. 2000, ApJ, 543, 644
Liu, M. C., Graham, J. R., & Charlot, S. 2002, ApJ, 564, 216
Luppino, G. A., & Tonry, J. L. 1993, ApJ, 410, 81
Ma, C.-P., Greene, J. E., McConnell, N., et al. 2014, ApJ, 795, 158
Macri, L. M., Stanek, K. Z., Bersier, D., Greenhill, L. J., & Reid, M. J. 2006, ApJ, 652, 1133
Marigo, P., Girardi, L., Bressan, A., et al. 2008, A&A, 482, 883
Marín-Franch, A., & Aparicio, A. 2006, A&A, 450, 979
Mei, S., Blakeslee, J. P., Côté, P., et al. 2007, ApJ, 655, 144
Mei, S., Blakeslee, J. P., Tonry, J. L., et al. 2005a, ApJS, 156, 113
Mei, S., Blakeslee, J. P., Tonry, J. L., et al. 2005b, ApJ, 625, 121
Mieske, S., Hilker, M., & Infante, L. 2003, A&A, 403, 43
Mieske, S., Hilker, M., & Infante, L. 2006, A&A, 458, 1013
Miyoshi, M., Moran, J., Herrnstein, J., et al. 1995, Natur, 373, 127
Mould, J. R., Huchra, J. P., Freedman, W. L., et al. 2000, ApJ, 529, 786
Pahre, M. A., & Mould, J. R. 1994, ApJ, 433, 567
Perlmutter, S., Aldering, G., Goldhaber, G., et al. 1999, ApJ, 517, 565
Pietrinferni, A., Cassisi, S., Salaris, M., & Castelli, F. 2004, ApJ, 612, 168
Pietrinferni, A., Cassisi, S., Salaris, M., & Castelli, F. 2006, ApJ, 642, 797
Pirzkal, N. 2014, The Near Infrared Sky Background, WFC3 Instrument Science Rep. 2014-11 (Space Telescope Science Institute)
Planck Collaboration, Ade, P. A. R., Aghanim, N., et al. 2015, A&A, submitted (arXiv:1502.01589)
Raimondo, G. 2009, ApJ, 700, 1247
Raimondo, G., Brocato, E., Cantiello, M., & Capaccioli, M. 2005, AJ, 130, 2625
Retzlaff, J., Rosati, P., Dickinson, M., et al. 2010, A&A, 511, A50
Riess, A. G., Filippenko, A. V., Challis, P., et al. 1998, AJ, 116, 1009
Riess, A. G., Macri, L., Casertano, S., et al. 2011, ApJ, 730, 119
Saha, A., Sandage, A., Labhardt, L., et al. 1996, ApJ, 466, 55
Saha, A., Sandage, A., Labhardt, L., et al. 1997, ApJ, 486, 1
Sakai, S., Mould, J. R., Hughes, S. M. G., et al. 2000, ApJ, 529, 698
Schlafly, E. F., & Finkbeiner, D. P. 2011, ApJ, 737, 103
Silbermann, N. A., Harding, P., Ferrarese, L., et al. 1999, ApJ, 515, 1
Sorce, J. G., Tully, R. B., & Courtois, H. M. 2012, ApJL, 758, L12
Stritzinger, M., Burns, C. R., Phillips, M. M., et al. 2010, AJ, 140, 2036
Thompson, R. I., Storrie-Lombardi, L. J., Weymann, R. J., et al. 1999, AJ, 117, 17
Tonry, J. L., Ajhar, E. A., & Luppino, G. A. 1990, AJ, 100, 1416
Tonry, J. L., Blakeslee, J. P., Ajhar, E. A., & Dressler, A. 1997, ApJ, 475, 399
Tonry, J. L., Dressler, A., Blakeslee, J. P., et al. 2001, ApJ, 546, 681
Tonry, J. L., & Schneider 1988, AJ, 96, 807
Trager, S. C., Faber, S. M., Worthey, G., & González, J. J. 2000, AJ, 119, 1645
van der Wel, A., Franx, M., van Dokkum, P. G., et al. 2014, ApJ, 788, 28
van Dokkum, P. G., Whitaker, K. E., Brammer, G., et al. 2010, ApJ, 709, 1018
Windhorst, R. A., Cohen, S. H., Hathi, N. P., et al. 2011, ApJS, 193, 27
Worthey, G. 1993, ApJ, 409, 530
Worthey, G. 1994, ApJS, 95, 107